Check for updates

Highly efficient, bioactive, and bifunctional sorbent p–n–p visible light heterogeneous photocatalyst utilizing ultra-fine ZnS nanoparticles embedded in a polymeric nanocomposite

Hanieh Bagheri,[a] Mohammad Akbarzadeh Pasha, [iD] *[a] Moslem Mansour Lakouraj, [iD] [b] Vahid Hasantabar[b] and Mojtaba Mohseni[c]

This study reports the successful synthesis of a ZnS@GO@Pani polymeric nanocomposite (NC) *via* chemical polymerization. The product was used for simultaneous photocatalytic degradation–adsorption of malachite green (MG), a carcinogenic and widely used dye. The physicochemical properties of the prepared NC were characterized by various techniques. Morphological and XRD results confirmed the fine size of ZnS nanoparticles (NPs) with an approximate mean size of 5 nm, uniformly distributed within the polymeric matrix. For comparative purposes, photocatalytic dye degradation–adsorption of this nanohybrid was explored both in the dark and under natural light. It was observed that 0.1 g of the ternary NC in MG aqueous solution (20 ppm) leads to dye adsorption within 15 minutes with an efficiency of 70% under dark conditions. Also, MG removal efficiency of up to 90% was achieved in 15 minutes under natural light owing to integrated photocatalytic degradation–adsorption mechanisms. Adsorption isotherm studies were performed considering Langmuir, Freundlich, Temkin, and Dubinin–Radushkevich (D–R) models. The results showed that the Freundlich isotherm with $R^2 = 0.988$ is well consistent with the experimental data. Integrated photocatalytic degradation–adsorption kinetics were modeled with pseudo-first-order (PFO) and pseudo-second-order (PSO) models where PSO with $R^2 = 0.999$ best fitted the data, implying the predominant role of chemical adsorption in the dye removal process. Antibacterial tests revealed superior antibacterial activity of the prepared ZnS@GO@Pani NC against both Gram-negative and Gram-positive bacteria, demonstrating the remarkable synergistic effect of ZnS NPs embedded in the GO@Pani matrix. Accordingly, the prepared NC could be regarded as a promising candidate for wastewater treatment applications. The leaching and regeneration studies also confirmed that the prepared NC is a non-toxic dye removal agent with good reusability.

1. Introduction

The rapid growth of industry and the release of large quantities of wastewater have increased environmental pollution. Wastewater may contain hazardous substances such as heavy metals, dyes, drugs, and complex chemical materials. Low biodegradability and high chemical stability of dyes have made them a serious environmental threat. In this regard, eliminating these pollutants from the environment is one of the most prominent goals for researchers. Different methods such as membrane filtration, coagulation, adsorption, and photocatalytic degradation have been used to remove organic dyes

from aqueous solutions.[1–4] This study aims to design an optimal nanostructured composite for fast and efficient dye removal from an aqueous solution based on both adsorption and photocatalysis mechanisms. Either adsorption and photocatalysis are surface phenomena. Therefore, surface characteristics such as the surface area and its chemistry play important roles in the adsorptive/photocatalytic removal of pollutants. In the adsorption process, the contaminant reacts with the adsorbent surface, based on the nature and properties of the adsorbent/adsorbate, to change the liquid/gas contaminant to the solid state. Nanosorbents are preferred over conventional adsorbents due to their high surface area, small size, adjustable surface properties, high adsorption capacity, high affinity, and nanoscale's improved magnetic, optical, and catalytic properties.[5] The dye adsorption mechanism by adsorbents is based on different interactions, including electrostatic interactions, π–π interactions, van der Waals forces, ion exchange, hydrogen bonding, and surface complexation. According to the literature,

[a]*Department of Solid-State Physics, Faculty of Basic Science, University of Mazandaran, 47416-95447, Babolsar, Iran. E-mail: m.akbarzadeh@umz.ac.ir*

[b]*Department of Organic Chemistry, Faculty of Chemistry, University of Mazandaran, Babolsar, 47416-95447, Iran*

[c]*Department of Molecular and Cell Biology, University of Mazandaran, Babolsar, 47416-95447, Iran*

various adsorbents have been employed to remove dyes from polluted water, including activated carbon, nanocarbon-based composites, polymeric composites, bio-adsorbents, and metal–organic framework (MOF).[5,6] On the other hand, photocatalysis relies on semiconductor materials to remove dye from aqueous solutions. The most significant photocatalysts are semiconductor metallic compounds, particularly metal oxides and sulfides like TiO_2, ZnO, NiO, CuO, MgO, CdS, and ZnS. Organic nanomaterials, such as carbon nanostructures and conducting polymers, have recently been employed as co-catalysts, gaining prominence in this field. The most critical challenges to using metallic compound photocatalysts are inactivity in visible light due to their wide bandgap and fast recombination of photogenerated electron/hole pairs. Bandgap engineering, which is accomplished by elemental doping or chemical surface modification of the semiconductor nanoparticle, has been proposed to address the problem of visible light inactivity.[5,7–9]

Additionally, heterogeneous photocatalysts have been proven to suppress electron/hole recombination and boost photocatalytic efficiency substantially. This kind of photocatalysts comes in various forms, including Schottky, plasmonic, p–n, and Z-scheme.[5,10] In a p–n heterojunction photocatalyst, an internal electric field is formed at the interfacial of the composite components, leading to effective electron/hole separation and severe repression of photoinduced charge pairs recombination. Polyaniline (Pani) is a conducting polymer that also serves as an effective sorbent with advantages including high effective surface area, high reactivity, high environmental stability, easy synthetic routes, cost-effectiveness, reusability, and thermal stability. Furthermore, due to their instinctive redox potential, high absorption coefficient in visible light, high mobility of charge carriers, visible range bandgap that can also be tuned chemically, and acting as an electron donor/hole acceptor, the fabrication of Pani-based nanocomposites (NCs) has been proposed to achieve better photocatalytic performance.[11] Various nanoparticles such as GO, rGO, Au, Fe_2O_3, ZnO, CdS, TiO_2, and ZrO_2 have been incorporated into Pani NCs to serve as adsorbents or photocatalysts in the removal of organic dyes.[12–15] Generally, carbon nanostructures, including carbon nanotubes, graphene (and its derivatives), and fullerene, have been widely used as supports of metallic compound photocatalyst NPs.[5,9] Among these nanocarbons, graphene provides better interfacial contact with the supported particle (due to its planar morphology), its production is simpler and less expensive, and it has much stronger absorption across the entire visible spectrum.[9] Furthermore, graphene provides a larger surface area because both sides of the sheet can be used for adsorption.[5,9] The combination of photocatalyst NPs and graphene in a composite brings a better performance through the mutual synergistic effect between graphene and photocatalyst NPs. The spatial confinement imposed by the supporting graphene plane and the large number of surface functional groups that act as anchor sites for the growth of photocatalytic NPs allows for improved dispersion of smaller photocatalyst NPs. In contrast, the presence of photocatalytic NPs prevents the accumulation of graphene planes,

enhancing the effective surface area. Additionally, due to its exceptional mechanical and chemical stability, graphene-supported photocatalyst provides an enhanced photostability for the composite.[5] Regarding operational cost and reusability, photocatalytic nanoparticles supported or immobilized on a suitable substrate such as nanocarbons or polymers have a clear preference over the powder form. Immobilization of photocatalytic NPs increases their quantum efficiency, facilitates their post-processing recovery, and reduces their loss in reuse.[9] Zinc sulfide (ZnS) has been utilized as a photocatalyst semiconductor NP due to its high thermal resistance, biocompatibility, and cost-effectiveness.[16] Owing to its high bandgap (3.6 eV), ZnS fails to absorb visible light. Its rapid electron–hole pair recombination can also result in a photo-corrosion reaction. Some studies have shown that the binding of broad bandgap metal sulfide semiconductors to graphene can promote their visible light activity. By serving as an electron transport channel, graphene can enhance the half-life of electron–hole pairs and the oxidation–reduction reactions on the surface of the composite nanostructure. In addition, graphene oxide (GO) helps the adsorption of contaminants thanks to its surface functional groups.[17–20] Single-functionality adsorbent or photocatalyst materials have been extensively investigated. However, few reports can be found on the bi-functionality materials that combine photocatalytic degradation and adsorption processes for the dye contaminant removal from aqueous solutions.[21–23] The term integrated photocatalyst–adsorbent (IPCA) designates an adsorbent capable of decomposing toxic compounds upon exposure to visible or ultraviolet light. These nanostructures retain all the interesting properties of their constituents and may also overcome some serious disadvantages such as low adsorption and rapid recombination of photo-generated electron/hole pairs. Pani is a p-type semiconductor and reductive photocatalyst (RP). GO is a p-type semiconductor, while ZnS is an n-type and wide bandgap semiconductor that can be considered both oxidative and reductive photocatalyst (OP and RP).[24–26] In combination with broadband semiconductor NPs, either graphene or polyaniline has been reported to operate as a photosensitizer, boosting the visible light responsiveness of the nanoparticles.[9] On the other hand, Pani and GO are effective sorbents due to their large surface areas and numerous surface functional groups.[27,28] As a result, a ternary heterostructure composed of Pani, GO, and ZnS NPs is expected to work simultaneously as an effective sorbent and a visible-driven photocatalyst. The current research is the first to describe a highly effective bi-functional sorbent that can operate as a p–n–p double type II heterogeneous photocatalyst for the quick and efficient removal of a hazardous organic pollutant (malachite green (MG)) from aqueous media.[29,30] The presence of Pani also reduces photo-corrosion of ZnS NPs upon exposure to light, hence, improving the stability of this new type of IPCA material.[31] The photocatalytic functionality of the designed NC is available under natural light without using any hazardous irradiation source. It also provides good reusability. As an interesting achievement, the proposed facile wet chemical method results in a Pani-based NC decorated by very fine zinc sulfide NPs (average size ∼ 5 nm) with

narrow size distribution. The metal sulfide–carbon–polymeric NC also exhibited excellent antibacterial activity against Gram-positive and Gram-negative bacteria. The synthesized ternary NC can be considered a remarkable candidate for wastewater treatment and environmental remediation due to these valuable properties.

2. Experimental

2.1. Materials

Zinc chloride ($ZnCl_2 \geq 98\%$), sodium sulfide (Na_2S, $\geq 97\%$), sodium dodecyl sulfate (SDS, $\geq 98\%$), hydrogen peroxide (30% H_2O_2), graphite powder($\geq 99.5\%$), sodium nitrate ($NaNO_3$, 99.99%), potassium permanganate ($KMnO_4$, $\geq 99\%$), hydrochloric acid (37% HCl), distilled aniline monomer($\geq 99.5\%$), and ammonium peroxy-di-sulfate (APS ($\geq 98\%$), serving as a radical oxidant for Pani), para-toluene sulfonic acid (p-TSA) ($\geq 98\%$), sulfuric acid (98% H_2SO_4), and ethanol (96%) were used to synthesize the ZnS@GO@Pani composite. All chemical reagents were of analytical laboratory grade and purchased from Merck and Sigma-Aldrich. They were used without further purification. Distilled water was used as a solvent in all reactions, and pure N_2 gas was purchased from Airgas (99.99%).

2.2. Characterization

The scanning electron microscopy (SEM; TESCAN MIRAIII, Czech) equipped with an energy-dispersive X-ray spectrophotometer (EDX; SAMX Detector) was employed to assess the morphology of the samples and recognize their elemental composition. Transmission electron microscopy (TEM, Philips EM208S 100 kV) was also used to further study the morphology and microstructure of the synthesized nanomaterials. Thermogravimetric analysis (TGA; TAQ50V6.3 Build 189 Germany) was also carried out at 25–600 °C and the heating rate of 20 °C min⁻¹ in the presence of argon gas. The Fourier transform infrared (FTIR) spectra were recorded by an FTIR spectrometer (BRUKER TENSOR27; Germany) using KBr pellets in the range of 600–4000 cm⁻¹. The crystalline structure and the approximate size of NPs were examined by X-ray diffractometer (XRD, Philips PW1730, Netherlands) at a scan rate of 10° min⁻¹. The alterations in the bandgap of the samples were explored by ultraviolet-diffuse reflection spectroscopy (UVDRS; Shimadzu, MPC-2200, Japan) in the wavelength range of 195 to 1100 nm. Dye removal performance, adsorption isotherms, and kinetics were measured using Cecil-5503 (Cambridge-England) UV-vis spectrophotometer. Brunauer–Emmett–Teller (BET; Belsorp II, Bell, Japan) analysis has been performed to determine the surface area and pore size of GO@Pani and ZnS@GO@Pani NCs. A dynamic light scattering (DLS) analyzer was used to assess the colloidal particle size distribution and surface charge of NPs (SZ-100z; Horiba Jobin Jyovin; United States). Gas chromatography-mass spectrometer (GC-MS) (Agilent 6890/5973N) equipped with a non-polar HP5 MS, 30 m × 0.32 mm × 0.25 μm was used in order to separate and identify the leaching by-products of NC solution in scan mode from a range of $m/z = 46$ to $m/z = 550$. Helium was used as carrier gas with 2.7

mL min⁻¹ flow. First, the column temperature was maintained at 50 °C for 4 minutes. It then rises to 190 °C with a rate of 7 °C min⁻¹. After that, the temperature was increased to 230 °C with a rate of 10 °C min⁻¹ and kept at this temperature for 5 min. The identification of by-products was carried out by comparing the obtained mass spectra with the NIST08 database. Atomic absorption analysis (NOV AA400P; Analytik Jena; Germany) was used to investigate the leaching of zinc ions.

2.3. Synthesis of GO@Pani and ZnS@GO@Pani NCs

ZnS NPs were synthesized according to our previous work, with significant modifications.[32] After mixing two aqueous solutions of zinc chloride (0.15 M) and sodium sulfide (0.15 M), the mixture was sonicated for 30 min, followed by adding 0.06 g SDS as a capping agent. After adjusting the pH to 5, the solution was stirred for 1 h at 60 °C. The resulting milky color product was separated through centrifugation at RCF of 3300g, washed continuously with distilled water, and finally dried in a vacuum oven at 50 °C for 24 h to obtain ZnS NPs. To synthesize ZnS@GO@Pani polymeric NC, 2.26 g of prepared ZnS NPs and 0.34 g GO (synthesized by Hummer's method) were dispersed in 150 mL distilled water using the sonication for 15 min to reach a monotonic dispersion. Under rapid stirring (1200 rpm), the pre-dissolved solution containing 6 mL aniline monomer in 20 mL distilled water and 0.9 g (p-TSA) acid were transferred to the above mixture as a dopant to protonate Pani. After measuring the pH of the solution (pH = 4), it was transferred to a 3-neck flask under N_2 gas in an ice bath and stirred for 2 h. The p-TSA acted as a dopant molecule composed of a hydrophilic ($SO_3^-H^+$) and a benzene ring that served as a hydrophobic group. Aniline monomer also contains a hydrophilic (NH_2) and hydrophobic (benzene ring) group; thus, p-TSA facilitates the interaction between the reactants during polymerization and contributes to the uniform growth of Pani grains on GO plates. APS solution (at APS : aniline molar ratio of 1 : 1) was added dropwise to the above mixture. Aniline and dopant molecules are assumed to be adsorbed on the surface of graphene; they are also susceptible to oxidation by APS. As a result, the mixture color changed to sludge green, indicating the polymerization of Pani. After stirring (for about 4 h), the precipitates were centrifuged (RCF = 4465g) and washed with distilled water and ethanol to remove unwanted species. Finally, the precipitates were dried in a vacuum oven at 70 °C for 12 hours. The synthesis of Pani (96% wt)@GO (4% wt) involved the same procedures as that of the ZnS (26%)@GO (4%)@Pani (70%) in the absence of ZnS. Unreacted monomers and Pani oligomers were eliminated by Soxhlet using water and ethanol for 24 h. Fig. 1 shows the ZnS@GO@Pani synthesis process.

2.4. Dye removal studies

Malachite green is a highly toxic, mutagenic, and tumor-stimulating dye. Although banned in many countries, it is widely used as an antiseptic to control fungal infections in many fish farms. The darkness condition was performed by a black box (35 cm × 25 cm × 22 cm) that could not be penetrated by light for the adsorption study. In the dye removal
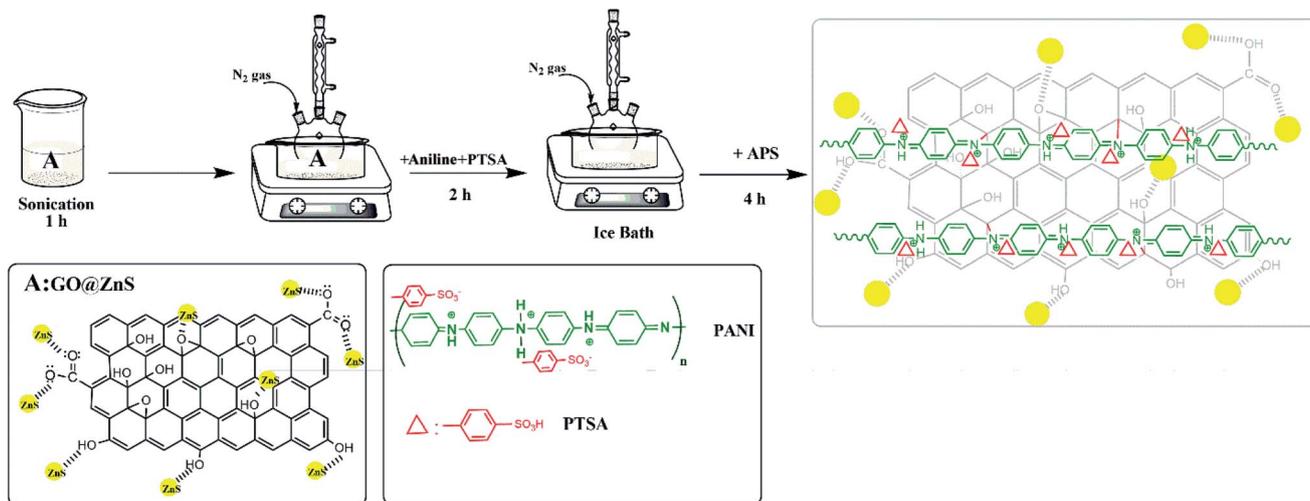
Fig. 1 Synthesis processes of ZnS@GO@Pani NC.

experiments, the following parameters were examined: (1) concentration effect: 0.05 g of NC was dispersed in 50 mL of MG aqueous solution (pH = 7, room temperature) with different concentrations (10, 20, 30, and 40 ppm). The solution was stirred for 45 min to determine the optimum concentration. (2) Effect of NC dosage: the different dosages of adsorbent (0.05, 0.1, 0.15, and 0.2 g) were dispersed in 50 mL of dye solution (20 ppm; pH = 7; room temperature) and stirred for 45 minutes to select the optimum adsorbent dosage. (3) Time effect: after determining the optimal concentration and dosage of adsorbent, 0.1 g of NC was dispersed in 50 mL of dye solution (20 ppm; pH = 7; room temperature) and stirred at different times (0, 5, 15, 30 and 45 min) to select the optimum time. (4) Temperature effect: in order to study the temperature effect, 0.1 g of the catalyst was dispersed in 50 mL of dye solution (20 ppm; pH = 7) at different temperatures (25, 35, 45, 55, and 65 °C) and stirred for 15 min.

The dye solution was stirred on a magnetic stirrer at 700 rpm in all stages. After separating the adsorbent from the dye solution by centrifugation, the residual dye concentration was determined by measuring the absorption of the solution at the wavelength of 616 nm using a UV-vis spectrometer. Adsorption capacity (Q_e; mg g^{-1}) and adsorption efficiency (η) were calculated according to the following equation:

$$Q_e = \frac{(C_0 - C_e)}{M} V \qquad (1)$$

$$\eta = \frac{(C_0 - C_e)}{C_e} \times 100 \qquad (2)$$

where C_0 and C_e are the initial and equilibrium concentrations of dye solution, respectively. M denotes the mass of NC, and V is the volume of solution. Additionally, to exploit the integrated photocatalytic degradation and adsorption of MG by the prepared ternary NC, the dye removal tests in natural light without direct sunlight were carried out during the day and inside the laboratory. The dye removal experiments related to

light conditions were conducted under the same parameters like the dark tests.

2.5. Antibacterial study

Kirby–Bauer disk diffusion test on the Mueller–Hinton agar was utilized to assess the antibacterial activity of the prepared samples against four types of Gram-positive and Gram-negative bacteria (*Staphylococcus aureus* ATCC 35923 (*S. aureus*) and *Bacillus subtilis* PTCC 1023 (*B. subtilis*), *Escherichia coli* PTCC 1330 (*E. coli*), and *Pseudomonas aeruginosa* PTCC 1074 (*P. aeruginosa*)). Gentamicin and chloramphenicol were considered reference antibiotics. In this test, 0.13 g of sample powder were prepared as tablets under the pressure of 14 MPa (diameter: 13 mm, thickness: 1 mm). After culturing the bacteria on Muller–Hinton agar, the tablets were placed on this medium and incubated at 37 °C for 24 h. The inhabitation zone was measured around each tablet.

3. Results and discussions

3.1. XRD study

The crystalline structure of NCs was determined by X-ray diffraction (XRD) analysis. Fig. 2 shows the XRD patterns of GO@Pani and ZnS@GO@Pani NCs. Two prominent diffraction peaks can be observed in GO@Pani NCs at $2\theta = 19.1°$ and $25.8°$, which belong to (010) and (200) planes of Pani, respectively. The emergence of these peaks can be assigned to the parallel and perpendicular periodicity of the Pani polymer chain.[33,34] The characteristic peaks of GO disappeared (a weak peak can be detected at $2\theta = 11.32°$)[35] which can be attributed to the exfoliation of GO layers in the NC matrix and also the small content of GO (4% W/W) in the NC structure. In the GO@ZnS@Pani NC spectrum, three diffraction peaks can be observed at $2\theta = 29.2°$, $48.2°$, and $57.6°$ corresponding to (111), (220), and (311) planes of face-centered cubic (FCC) crystal phase of ZnS NPs. The d-spacing values of Pani in GO@Pani and ZnS in ZnS@GO@Pani
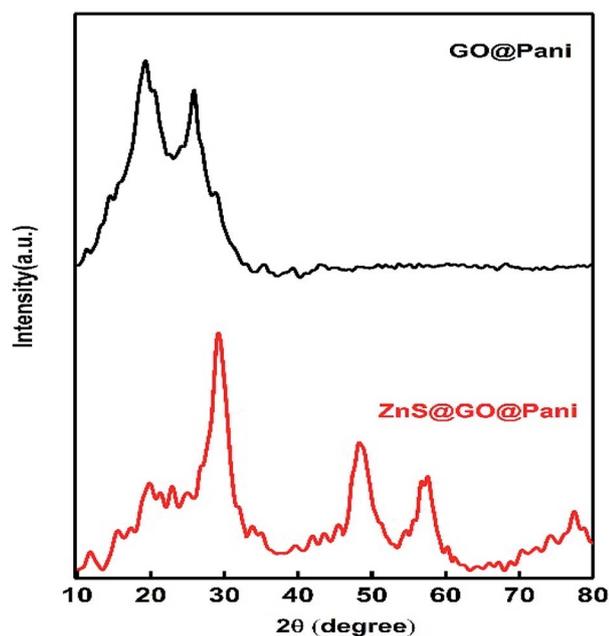
Fig. 2   The XRD spectra of GO@Pani and ZnS@GO@Pani NCs.

were calculated by Bragg's equation (eqn (3)), for $n = 1$ as summarized in Table 1:

$$d_{hkl} = n\lambda/2 \sin \theta_{hkl} \qquad (3)$$

Based on eqn (4), the average lattice parameter of ZnS NPs was calculated as $a_0 = 5.3080$ Å:

$$a_0 = d_{hkl}(h^2 + k^2 + l^2)^{1/2} \qquad (4)$$

and the inter-chain separation length of Pani was determined based on the equation presented by Klug and Alexander:

$$R = 5\lambda/(8 \sin \theta) \qquad (5)$$

This parameter showed a decrease from 4.312 to 3.819 Å due to ZnS NPs, implying higher compactness of the polymer chains in the GO@ZnS@Pani structure compared to GO@Pani.[36] According to the X-ray pattern of ZnS NPs recorded in our previous work, the characteristic peaks exhibited a slight shift which could be due to the formation of NPs in the Pani matrix

Table 1 d-Spacing (d_{hkl}), inter-chain separation length (R), and crystallite size of GO@Pani and ZnS@GO@Pani NCs derived from XRD patterns

Sample name	2θ	hkl	d_{hkl} (Å)	R (Å)	The crystallite size (nm)
ZnS@GO@Pani	29.2	(111)	3.055	3.82	3.7 (ZnS)
	48.2	(220)	1.885		
	57.6	(311)	1.598		
GO@Pani	25.8	(200)	3.449	4.31	4.5 (Pani)
	19.1	(010)	4.641		

as a result of the changes in bond length and bond stretching in the composite.[32,36] On the other hand, the intensity of the peaks related to GO and Pani in GO@ZnS@Pani decreased, which can be due to the predominance of the crystalline structure of ZnS NPs over the quasi-crystalline structure of GO@Pani. Based on the Debye–Scherrer equation (eqn (6)), the size of Pani crystallites in GO@Pani NC and ZnS crystallites in ZnS@GO@Pani NCs were 4.5 and 3.7 nm, respectively:

$$D = K\lambda/\beta \cos \theta \qquad (6)$$

where λ shows X-ray wavelength (Cu K$_\alpha$ = 1.54 Å), k is a dimensionless shape factor (usually considered 0.9), D denotes the average size of crystallites, β represents the full width at the half-maximum of a diffraction peak in radian (FWHM), and θ stands for the Bragg angle.

3.2. FTIR study

The surface chemistry and functional groups of the synthesized samples were examined by FTIR spectroscopy. Fig. 3 shows the spectra of GO as well as the binary and ternary NCs. Based on Table 2, in the GO spectrum, the broadband centered in 3400 and the bands at 1727 and 1610 cm^{-1} correspond to the hydroxyl groups in water, C=O stretching vibration in carboxylic acid, and C=C bond in aromatic rings, respectively. Moreover, the peak at 1215 cm^{-1} belongs to the C–O stretching vibrations of epoxy groups in the GO structure.[32] The peak emerging at 1049 cm^{-1} can be attributed to the stretching vibration of the etheric bond.[37–39] The presence of these oxygen functional groups indicates the proper oxidation of GO.[35] Concerning the spectrum of GO@Pani with 4 wt% GO content, the band at 3436 cm^{-1} corresponds to the hydrogen bond between the NH group of Pani and the OH group of GO. Besides, the appearance of peaks at 1499 and 1582 cm^{-1} can be assigned to C=C stretching of the benzenoid and quinonoid rings of polymer chains in Pani, respectively.[34] Furthermore, a sharp
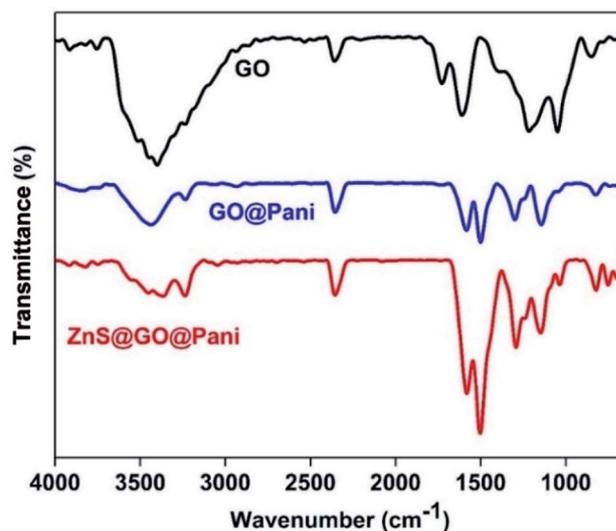

Fig. 3   FTIR spectra of synthesized nanostructures.

Table 2 A summary of FTIR results of the synthesized samples

Item	GO (cm^{-1})	GO@Pani (cm^{-1})	ZnS@GO@Pani (cm^{-1})	Functional groups
1	3400	3436	3370	Stretching OH & NH
2	—	3235	3235	NH stretching of Pani
3	1727	—	—	C=O stretching
4	1610	—	—	C=C in aromatic rings
5	—	1582	1579	C=C stretching of Pani quinonoid ring
6	—	1499	1502	C=C stretching of Pani benzenoid ring
7	1215	—	—	C–O stretching in epoxy
8	1049	—	—	Stretching vibration of etheric bond
9	—	1143	1147	C–N stretching vibration in benzenoid ring
10	—	1299	1290	C–N stretching of the secondary amine
11	—	824	822	*Para* substitutions in benzene ring

peak at 1299 cm^{-1} belongs to the C–N stretching of secondary amine, while the peaks at 3235 and 1143 cm^{-1} indicate NH stretching of Pani and C–N stretching vibration in the benzenoid ring of Pani, respectively.[33] In the spectrum of ZnS@GO@Pani, the intensity of GO peaks showed a dramatic reduction relative to GO and GO@Pani, as NC is mainly composed of Pani segments. A decrement in the intensity of OH and NH groups in this NC can be attributed to the coordination with ZnS NPs. According to Table 2, some common peaks of GO@Pani and ZnS@GO@Pani NCs exhibited a slight shift

(items of 5, 6, 9, 10, 11), which can be ascribed to the dispersion of ZnS NPs in the graphene–polymer matrix.[40,41] The peak at 697 cm^{-1} can be attributed to the Zn–S bond in ternary NC.[42] Furthermore, the intensity of benzenoid and quinonoid rings showed a significant increase in ZnS@GO@Pani compared to GO@Pani. In the absence of ZnS NPs, electrostatic repulsion occurs between the Pani chains with similar charges.[43] In the ternary NC, however, the interchain spaces between these chains declined due to the electrostatic interaction of sulfide ions of ZnS NPs and ammonium sites. These observations are
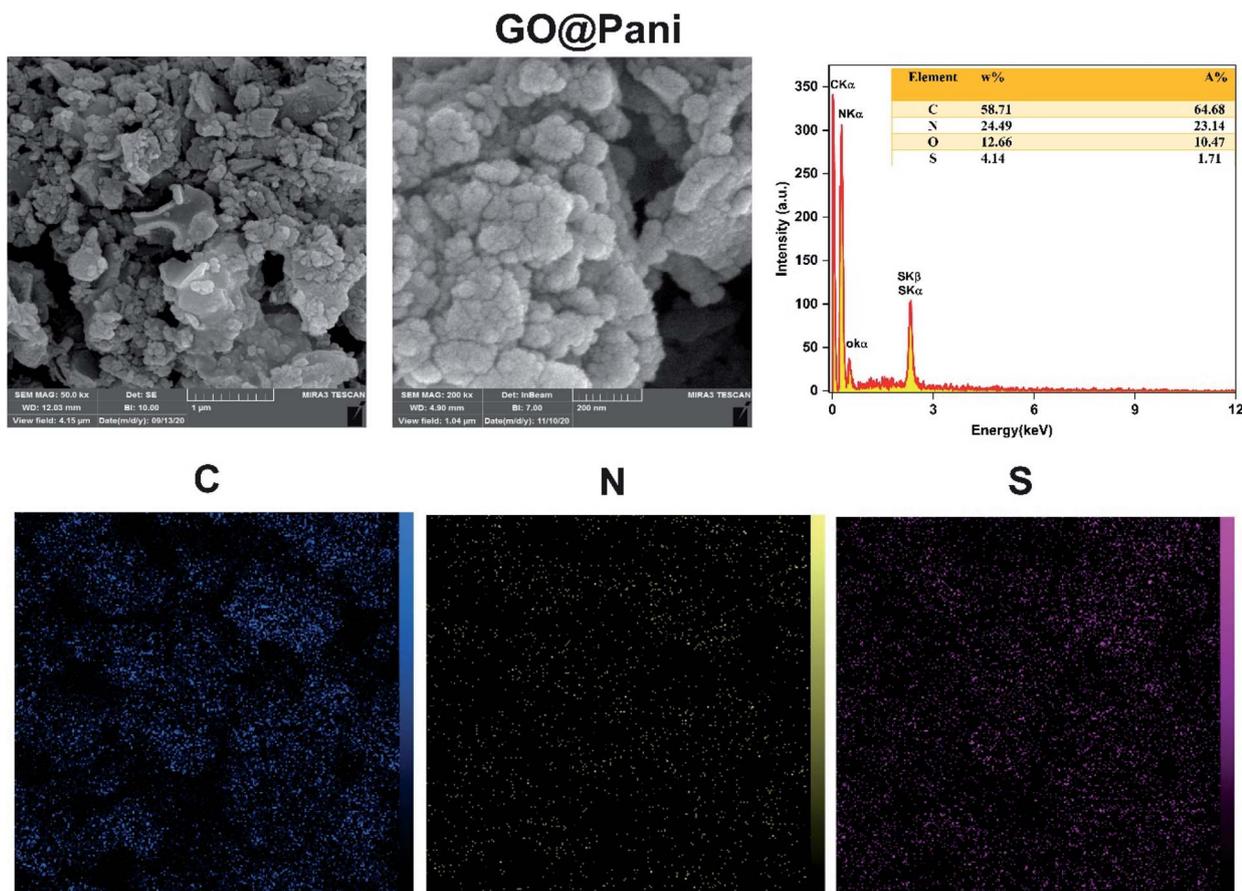

Fig. 4 FESEM images, EDX, and X-map analysis of GO@Pani composite.

consistent with the XRD results indicating decreasing the interchain separation length in ternary NCs compared to the binary NC, implying improved Pani formation and longer chains in ZnS@GO@Pani.

3.3. Morphological studies and elemental composition

GO is a non-stoichiometric two-dimensional honeycomb carbon structure with oxygen-containing functional groups, especially on its edges. These areas are suitable sites for Pani polymerization at the surface of GO. In addition, stacking force and hydrogen bonding favor Pani nucleation on the surface of GO. The FESEM images of GO@Pani and ZnS@GO@Pani NCs are shown in Fig. 4 and 5. As can be seen, GO@Pani had a cauliflower-like aggregate structure. The presence of ZnS NPs at the ZnS@GO@Pani NC matrix altered the morphology of NC from granular to a planar structure composed of a more uniform dispersion of small NPs. As mentioned in the XRD result, the polymer chains of the ZnS@GO@Pani structure are more compact compared to GO@Pani, due to the presence of
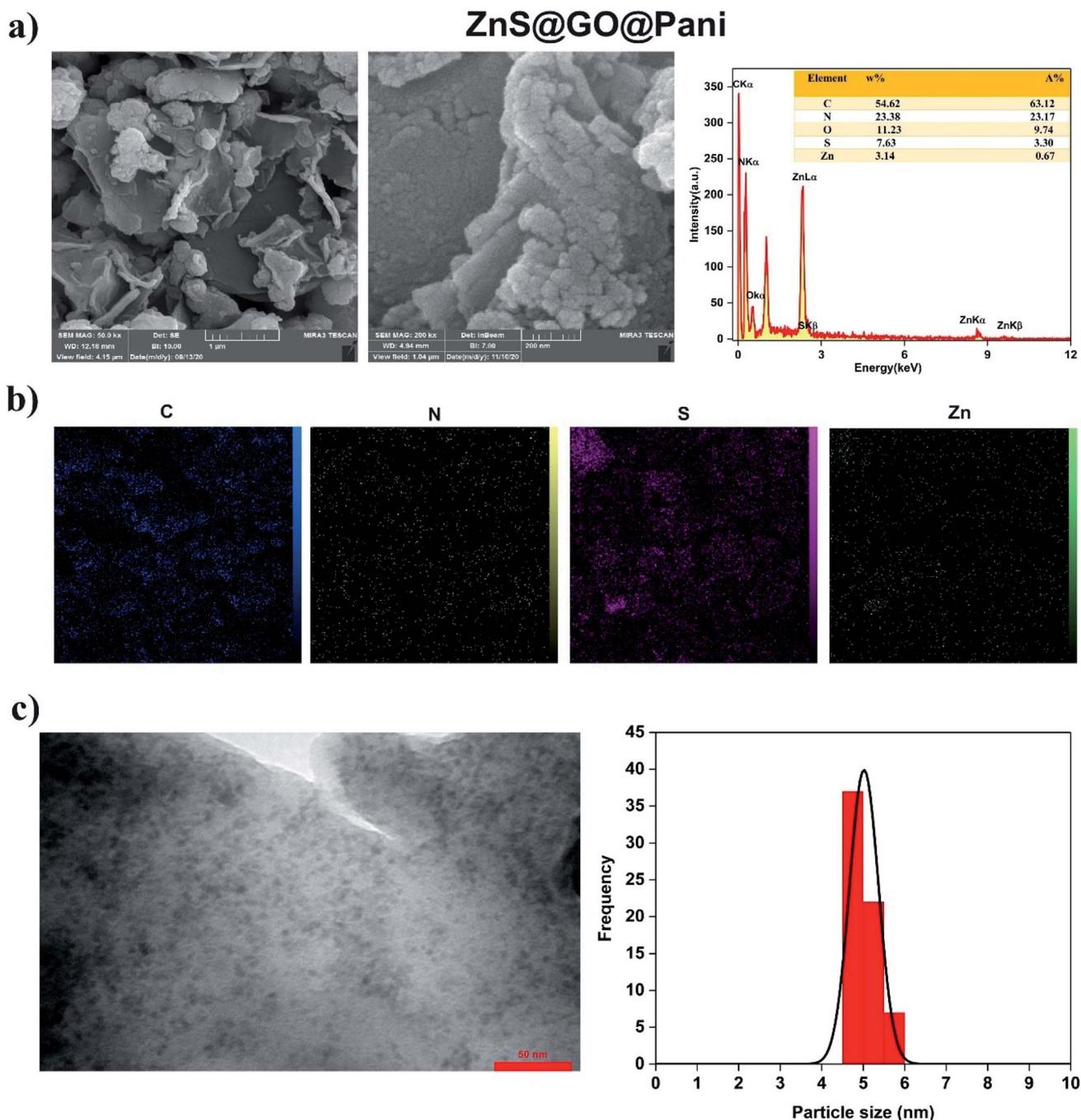

Fig. 5 ZnS@GO@Pani NC characterization (a) FESEM images (low and high magnifications) and EDX analysis, (b) elemental X-map distribution, and (c) TEM image and ZnS particle size distribution histogram.

ZnS NPs, which may promote the formation of the mentioned planar morphology. EDX analyses were also employed to assess the elemental composition of the samples. As seen in Fig. 4 and 5, carbon has the highest weight percentage in both samples since Pani and GO are carbon-rich compounds. Moreover, the dopant molecules also encompass some carbon atoms. The presence of Zn in ZnS@GO@Pani NC and a relative increment in the sulfur content (from 1.71 to 3.30 A%) could be assigned to the grafting of ZnS NPs to the ternary polymeric NC. Moreover, the X-map of the elemental distribution can be found in Fig. 4 and 5 reveal the spatial distribution of the expected elements in the synthesized NCs. As can be seen, the distribution of carbon was denser in GO@Pani compared to ZnS@GO@Pani, which could be due to the higher carbon content of the matrix of the binary composite. The sulfur map of the GO@Pani was more uniform than the ZnS@GO@Pani. Besides, the map of this element in ZnS@GO@Pani showed a cluster pattern, which can be a consequence of the presence of ZnS NPs. Noteworthy, the X-map of Zn revealed its homogeneous distribution, reflecting the uniform spreading of ZnS NPs in the matrix of ternary NC, which is in good accordance with TEM observations.

TEM was used to confirm the hierarchical and fine structure of the ternary NC, as shown in Fig. 5(c). The dark spots represent the small ZnS NPs in the polymeric substrate. The narrow particle size distribution implied the size homogeneity of ZnS NPs. Based on this histogram, the average size of ZnS NPs was 5.02 ± 0.7 nm ($\bar{d} \pm \sigma$), demonstrating proper consistency with the Debye–Scherrer-estimated crystallite size. Therefore, the proposed wet chemical method can result in a Pani-based NC decorated by very fine zinc sulfide NPs with uniform size spreading. Furthermore, this image confirms the successful grafting of ZnS NPs to the GO@Pani matrix.

3.4. Thermal study

The thermal stability and the patterns of thermal degradation can be well explored by thermal analysis. The TGA thermograms of the GO@Pani and GO@ZnS@Pani are displayed in Fig. 6(a). In line with previous works,[32] a three-step weight loss can be observed in both patterns. In the case of GO@Pani, the first stage of weight loss (6%) occurred below 150 °C, which can be assigned to the evaporation of water and moisture content as well as water entrapped in the NC structure. The second weight loss (10%) can be detected at 150–330 °C, corresponding to the removal of (i) reactive functional groups such as O–H, C–O, and –COOH, (ii) volatile spices attached to the Pani polymeric chains, and (iii) dopant release from Pani backbone.[41,44,45] The third weight loss was a rapid mass drop (23%) at 330–600 °C, which can be attributed to the thermal decomposition of the Pani matrix, breaking of its backbone, the loss of the covalent bonds between GO and Pani, and destruction of GO carbon rings.[46] Compared with the TGA diagram of pure Pani in the literature, the prepared GO@Pani sample showed higher thermal stability (*i.e.*, higher decomposition temperature and char yield) as binding of Pani with GO resulted in the homogeneous dispersal of GO in a polymeric matrix. The strong interaction between these counterparts can be explained through π–π stacking forces and hydrogen bonds between amino groups of Pani and the hydroxyl groups of GO.[47]

The ZnS@GO@Pani showed a similar three-step weight loss pattern but at smaller drops. The first (4 wt%), second (8 wt%), and the third (18 wt%) weight losses occurred below 150 °C, 150–300, and above 300 °C, respectively. Additionally, the third step of weight loss in the ZnS@GO@Pani NC occurred due to the elimination of the interaction between ZnS NPs and the GO@Pani matrix. The char yield of GO@Pani and ZnS@GO@Pani NCs was 60.7% and 70.1%, respectively, suggesting a significantly higher thermal stability of ZnS@GO@Pani NC. Such higher thermal stability can be assigned to the coordination of ZnS NPs by GO@Pani counterpart and embedding of these NPs in the mesoporous structure of the NC. DTA diagrams of the two NCs (Fig. 6(b)) showed an endothermic peak at 83.2 °C and 72.7 °C for GO@Pani and ZnS@GO@Pani, respectively; both of which can be attributed to the loss of water. Moreover, a broad exothermic peak centered at about 430 °C in both NCs, is related to the gradual decomposition of Pani chains and destruction of GO structure, as mentioned in the
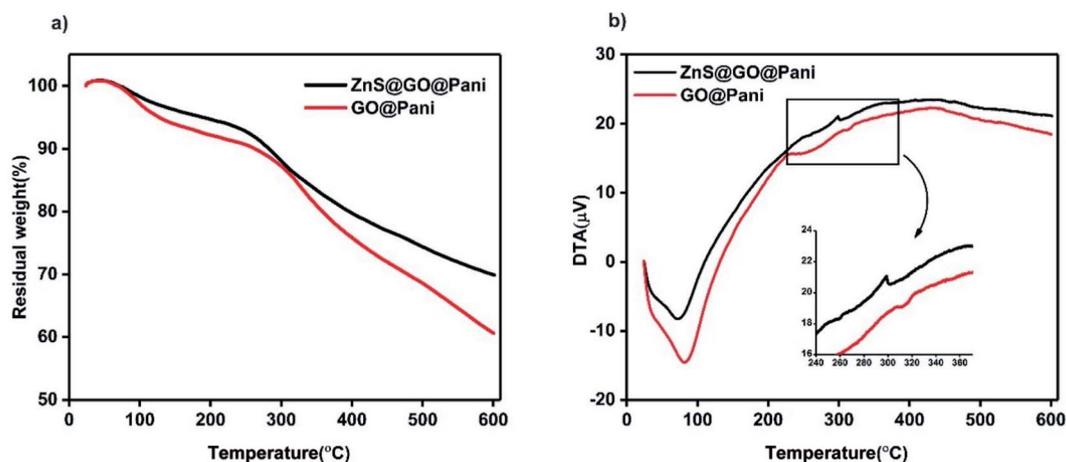

Fig. 6 Thermogravimetric analysis (a) TGA curves and (b) DTA curves of GO@Pani & ZnS@GO@Pani NCs.

third step of weight loss observed in TGA analysis.[44] In addition, a sharp exothermic peak at 299 °C in the DTA curve of ZnS@GO@Pani, could be assigned to the release of ZnS NPs from graphene oxide–polymeric texture.

3.5. Bandgap study

Regarding the importance of optical parameters, the DRS analysis was used to derive the bandgap of GO@Pani and ZnS@GO@Pani NCs, as presented in Fig. 7. Photons with energies higher than the bandgap energy can be absorbed and excite electrons of the valence band to the conduction band. The optical bandgap (E_g) can be determined by the Tauc relation:

$$(\alpha h\nu)^{1/n} = A(h\nu - E_g) \tag{7}$$

where α, $h\nu$, and A refer to the absorption coefficient, photon energy, and a constant, respectively, n is a constant equal to 0.5 for a direct bandgap and 2 for an indirect optical bandgap. Here, $n = 0.5$ was used for direct electronic transitions. As shown in Fig. 7, the bandgap of GO@Pani and ZnS@GO@Pani samples was evaluated 2.76 and 2.72 eV, respectively, reflecting the

photoactivity of these Pani-based NCs under visible light. A slight reduction can be detected in the bandgap upon incorporating ZnS NPs into the GO@Pani sample. The bandgap of the prepared GO@Pani matched with the one of pure Pani, probably due to the small amount of GO (4% wt) in the binary polymeric composite. Doping and surface modification are two main factors in the bandgap engineering of materials.[48] In line with the XRD results, the presence of ZnS NPs decreased the interchain separation of Pani, causing the strong interactions between these counterparts, resulting in tension within the Pani lattice structure and eventually a slight bandgap narrowing.

3.6. BET analysis

Fig. 8 presents the N_2 adsorption–desorption isotherms of GO@Pani and ZnS@GO@Pani samples at 77 K. These curves correspond to the type II isotherms of IUPAC classification with slight hysteresis of type H3.[49,50] The mentioned isotherm indicates the mesoporous structure of the NCs. The H3 hysteresis loop indicates pores with slit geometry resulting from agglomerates of parallel plate-shaped particles as expected based on the morphological study of the prepared NCs. Mesoporous materials have pores with diameters ranging between 2 and
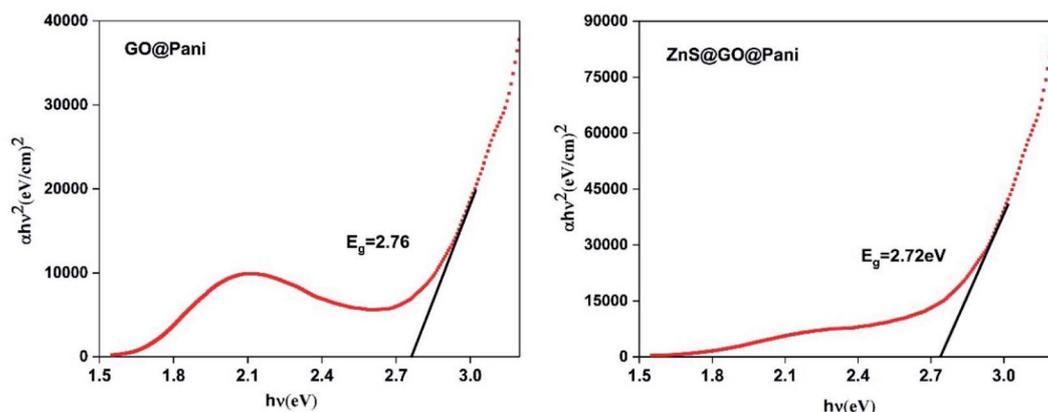

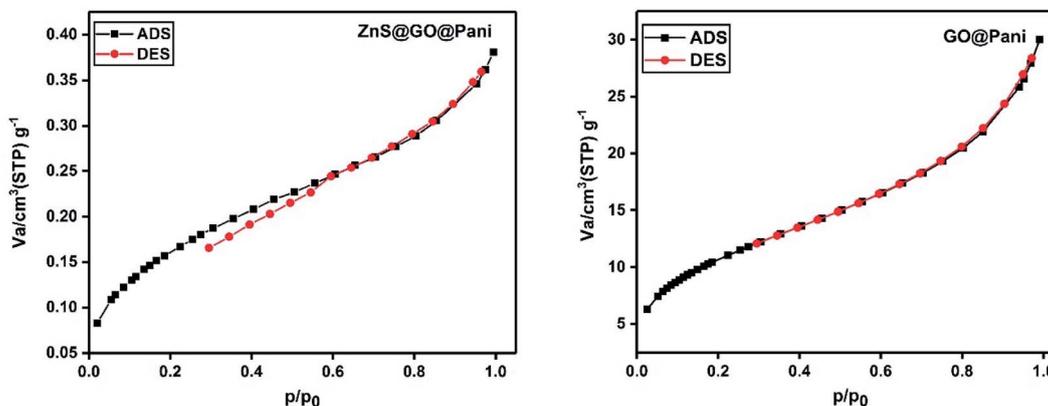**Fig. 7** Tauc plots for bandgap determination of GO@Pani and ZnS@GO@Pani NCs.

Fig. 8 N$_2$ adsorption–desorption isotherms of GO@Pani and ZnS@GO@Pani NCs.

Table 3 Data derived from BET study of GO@Pani, and ZnS@GO@Pani NCs

	GO@Pani	ZnS@GO@Pani
Mean pore diameter (nm)	4.79	3.90
Surface area (m^2 g^{-1})	38.65	0.598
Total pore volume (cm^3 g^{-1})	0.046	0.0006

50 nm, matching the mean pore diameters of the prepared binary and ternary NCs. As shown in Table 3, the average pore diameter, BET specific surface area, and total pore volume of ZnS@GO@Pani showed a drastic decrease compared to GO@Pani. This result is consistent with XRD analysis and SEM and TEM observation and can be attributed to the penetration of ZnS NPs onto the mesoporous texture of GO@Pani. The planar structure of ternary composite, in contrast to the granular morphology of binary composite and a decrease in the separation length of Pani chains (observed in the XRD result), can explain this difference. ZnS NPs were mainly encapsulated in the body of the GO@Pani matrix, while a minor part of them became immobilized on the surface of the binary one. The mean pore diameter of GO@Pani was evaluated to be 4.79 nm, very close to the average size of ZnS NPs derived from TEM observation, 5.02 nm, which can support the idea of embedding ZnS NPs into the porous texture of GO@Pani composite.

3.7. Dynamic light scattering (DLS) and zeta potential

The stability, electrostatic and dynamic behavior of nano and micron-sized particles are studied using DLS analysis.[51] The particle size distribution and zeta potential of charged colloids can be determined based on light scattering. Due to Brownian motion, the local density of suspended particles fluctuates temporarily in a colloid. As a result, the intensity of light scattered by the colloid fluctuates, which is dependent on the diffusion constant of the suspended particles. The hydrodynamic radius of the suspended particles can be extracted from the diffusion constant. It is noteworthy that the particle size in liquids and solutions is generally much larger than their actual sizes due to the interaction between the functional groups on the surface of the NPs and other species in the solution, like solvent molecules.[52] Fig. 9 shows the colloidal size distribution diagram of synthesized NPs and their NCs. According to the results in Table 4, the average hydrodynamic size of ZnS, GO, Pani, Pani@GO, and ZnS@Pani@GO are 16, 29, 20, 220, and 377 nm, respectively. Zeta potential is used to estimate colloidal particles' surface charge and surface potential. If the dispersed particles have a high zeta potential ($\geq \pm 30$ mV), a strong repulsive intraparticle force prevents their accumulation, indicating a stable dispersion, while a low zeta potential ($\leq \pm 30$ mV) indicates an unstable dispersion.

Due to the obtained zeta potentials, the colloids of ZnS, GO, and Pani NPs (the composite components) are stable. The surface charge of these particles is negative. The zeta potential values observed are in agreement with previous studies.[53–55] GO colloid has the highest zeta potential, which is expected given many oxygen-containing functional groups on its surface. The ternary NCs zeta potential is higher than the binary one. Furthermore, based on their values, the ternary NC colloid appears to be significantly more stable than the binary one.
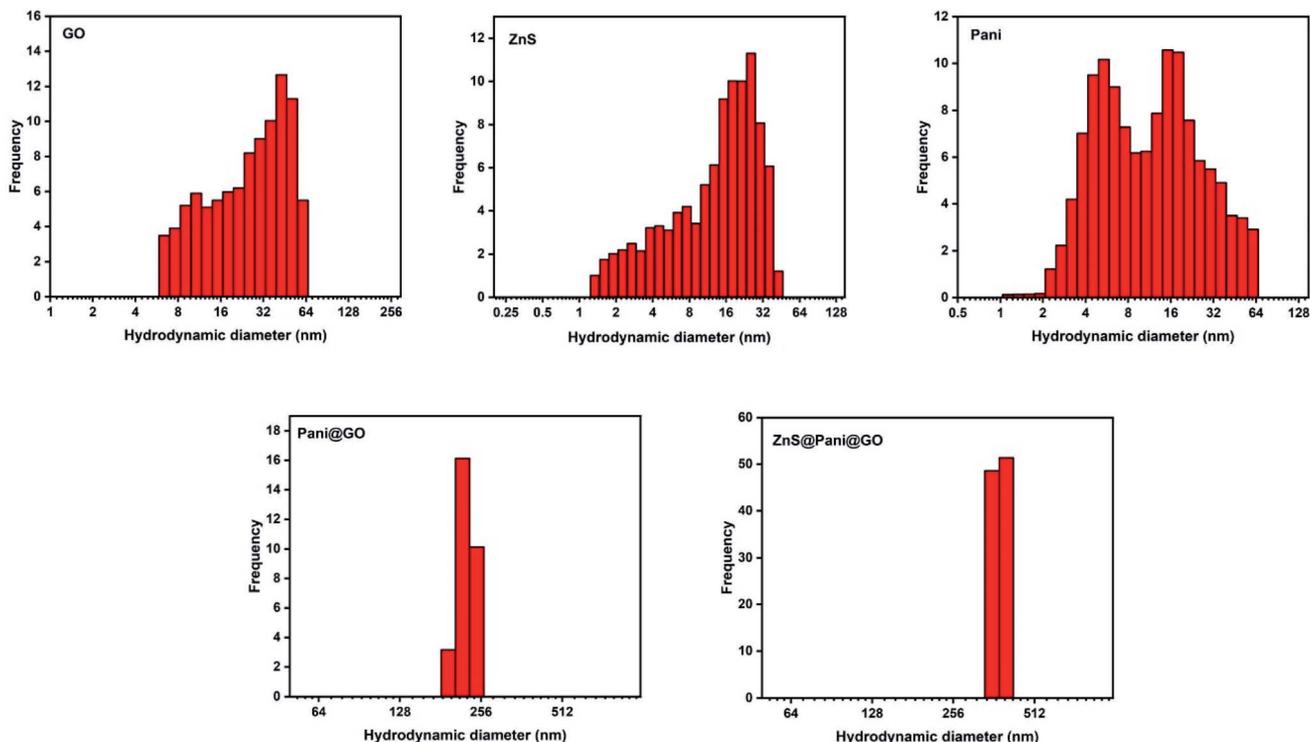

Fig. 9 Dynamic light scattering (DLS) studies of synthesized GO, ZnS, Pani NPs, and their NCs.

Table 4 The zeta potential and average hydrodynamic size of synthesized NPs and their NCs

Specimen	Zeta potential (mV)	The average hydrodynamic size (nm)
ZnS	−31.3	16
Pani	−33.8	20
GO	−54.2	29
Pani@GO	−23.5	220
ZnS@Pani@GO	−38.4	377

3.8. MG removal from aqueous solution

Compared to the binary GO@Pani, the ZnS@GO@Pani NC exhibited several interesting features such as ternary structure benefiting three synergetic counterparts, higher thermal stability, narrower bandgap, significantly higher surface charge and zeta potential (making the ternary NC colloid very more stable), excellent antibacterial property (further presented), and the presence of very fine sizes of zinc sulfide NPs. Therefore, the bi-functional adsorption–photocatalysis behavior of this NC was explored in an aqueous solution of MG. The evaluated parameters included initial dye concentrations (10, 20, 30 and 40 ppm), contact time (5, 15, 30 and 45 min), NC dosage (0.05, 0.1, 0.15, and 0.2 g) and temperature (25, 35, 45, 55 and 65 °C). All experiments were carried out in triplicates, and the average was reported.

3.8.1. Effect of the initial dye concentration. The adsorption behavior of the adsorbent has been dependent on the initial dye concentration. So, the effect of dye concentration was studied on dye removal efficiency at room temperature. The pH of the dye solution was 7 (neutral), and the NC dosage was considered 0.05 g with a 45 minute contact time. Fig. 10 shows the UV-vis spectra of different concentrations of MG solution after exposure to polymeric NCs in darkness and under natural light. The MG concentration of 20 ppm was selected as the optimal concentration with a removal percentage of 70% in darkness (attributed only to the adsorption mechanism) and
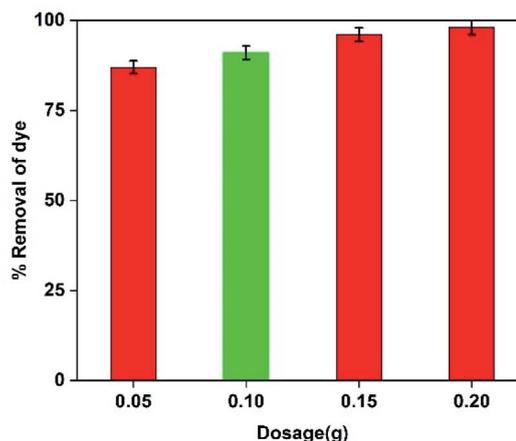

Fig. 11 The effect of ternary NC dosage on MG adsorption process.

86% under natural light (integrated absorption and photocatalysis activities). Regarding the abundance of active sites in NC, the adsorption effect decreases with increasing initial dye concentration as the entire surface of the adsorbent will be covered by dye molecules, weakening the adsorbent interactions. In other words, the electrostatic interaction at the adsorbent site decreased by enhancing the initial concentration, hence declining the affinity of the dye to the adsorbent.[56] On the other hand, increasing dye concentration blocks the light absorbance of the photocatalyst, decreasing the rate of photoexcited electron–hole generation and consequently the photocatalytic degradation of dye molecules.

3.8.2. Effect of NC dosage on the adsorption process. The effect of ternary polymeric NCs dosage on the MG adsorption was investigated, as shown in Fig. 11. A rise in the adsorbent dosage from 0.05 to 0.1 g enhanced the adsorption rate to 92%. Further increase of the adsorbent dosage to 0.2 g incremented dye adsorption only by 6% (reach 98%), which means the adsorption percentage of the dye remained almost constant.
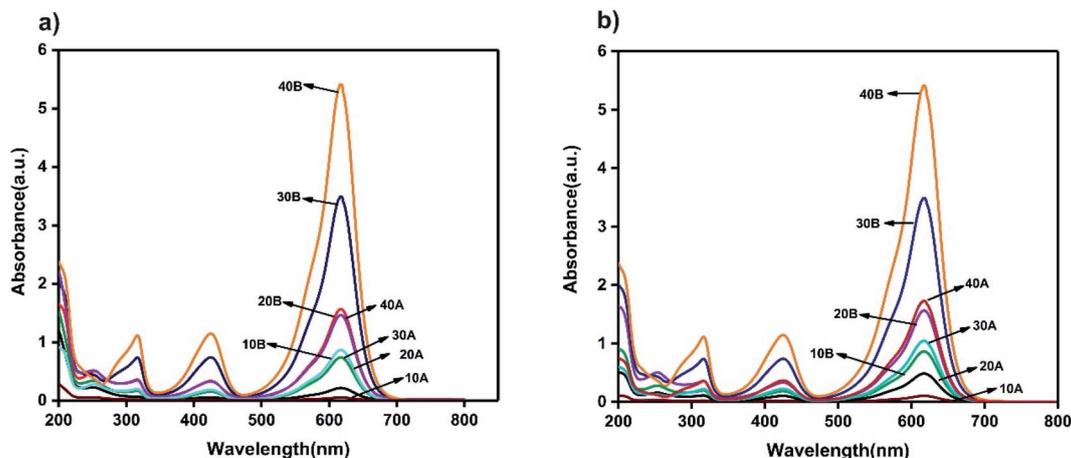

Fig. 10 Effect of dye concentration on the removal process at (a) light and (b) dark conditions. B and A imply before and after treatment, respectively.
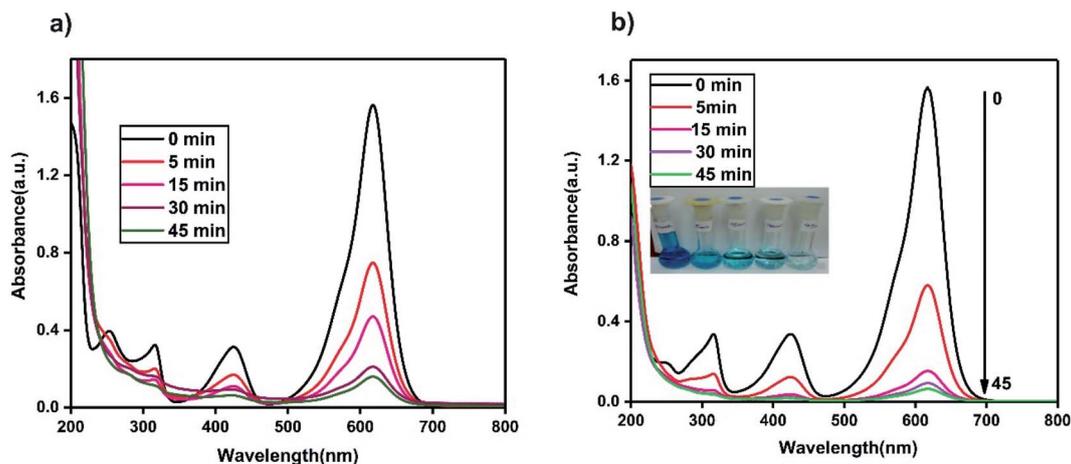
Fig. 12 The effect of contact time on the MG removal process under (a) darkness and (b) light.
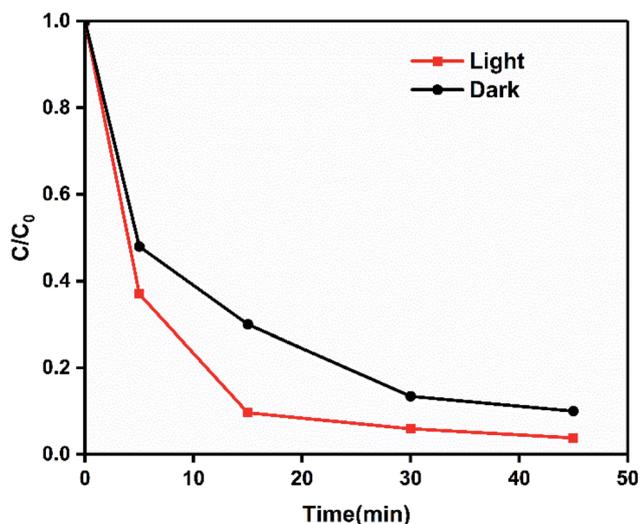

Fig. 13 The plot of dye concentration C/C_0 versus time in the presence of ternary NC in darkness and illumination.

This trend can be attributed to the relative accumulation of adsorbent particles. On the other hand, the dye density is constant, leaving many adsorption sites empty and unused. Thus, the adsorbent dosage of 0.1 g was considered the optimal value.

3.8.3. Effect of contact time. The effect of contact time was assessed using 0.1 g of NC and 50 mL of dye solution at a concentration of 20 ppm, and the results can be found in Fig. 12. The MG removal using ZnS@GO@Pani NC was very fast at the beginning of the process, *i.e.*, 90% of MG dye was removed in the first 15 minutes (light condition). The process then proceeded slowly, and the dye removal of 96% was achieved after 45 minutes. Thus, a contact time of 15 minutes was selected as the optimum value. Based on Fig. 13, a decline in the C/C_0 ratio indicates an increase in dye removal. The reduction rate of dye concentration under light was significantly greater than that of the dark condition, which can be due to the integrated photocatalytic activity of the ternary NC.

3.8.4. Effect of temperature. The temperature effect is one of the important parameters in the adsorption and removal of pollutants from the aquatic environment. Increasing the
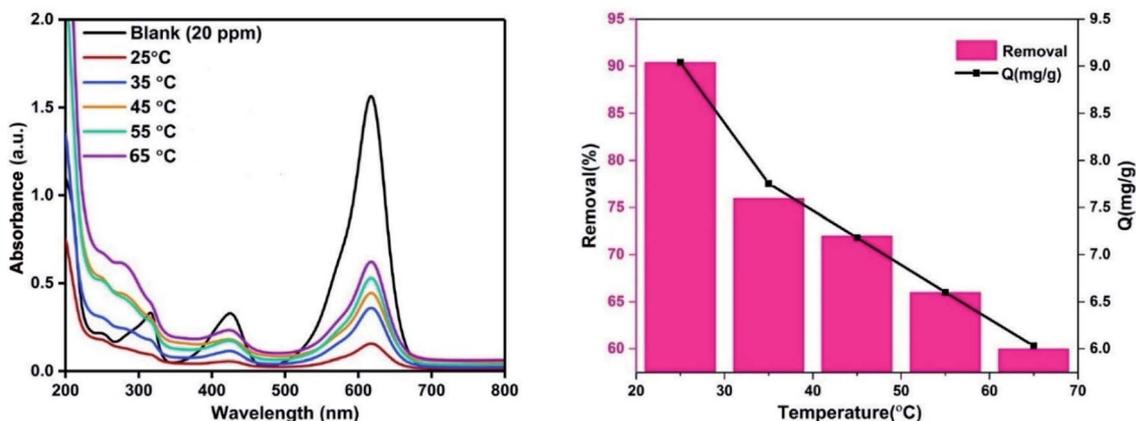

Fig. 14 The effect of temperature on MG removal in light condition.

temperature increases the adsorbate molecules' diffusion rate, reduces the solution's viscosity, and changes the adsorption capacity. In order to study the temperature effect on the removal of MG from the aqueous solution, 0.1 g of NC was dispersed in 50 mL of solution (20 ppm; pH = 7) at different temperatures (25, 35, 45, 55, and 65 °C), and the removal percentage and adsorption capacity were investigated. As shown in Fig. 14, increasing the temperature of the dye solution reduced the dye removal, indicating the exothermic nature of the reaction. This increase in temperature reduces the gravitational force between the dye molecules and the adsorbent surface and weakens the physical bonds.[57,58] On the other hand, the physical bonds between the dye molecules and water will be stronger than their bonds with the adsorbent surface[59] so the adsorption capacity will be reduced.

3.8.5. Adsorption isotherm study. Adsorption isotherm curves are valuable tools describing the phenomena governing the adsorption or desorption processes in the aquatic environment at a constant temperature and pH. In the darkness, the removal of MG is an adsorption-based process. Thus, dye

removal data under darkness was used to study the adsorption isotherms. In this study, Langmuir, Freundlich, Temkin, and Dubinin–Radushkevich (D–R) models were employed to evaluate the equilibrium data to clarify the adsorption mechanism, properties of the adsorbent surface, and adsorption of contaminants. In the Langmuir model, the adsorption process occurs at specific homogeneous sites within the adsorbent. It is assumed that whenever a dye molecule occupies a site, no other adsorption can occur at that location.[60] This model is thus suitable for monolayer adsorption processes. In this model, all molecules have constant activation and enthalpy energy, implying that all adsorption sites have the same adsorption affinity. Adsorbate molecules are assumed to be non-interactive. The mathematical expression of the Langmuir model is as follows:[61]

$$C_e/q_e = 1/K_L Q_m + C_e/Q_m \quad (8)$$
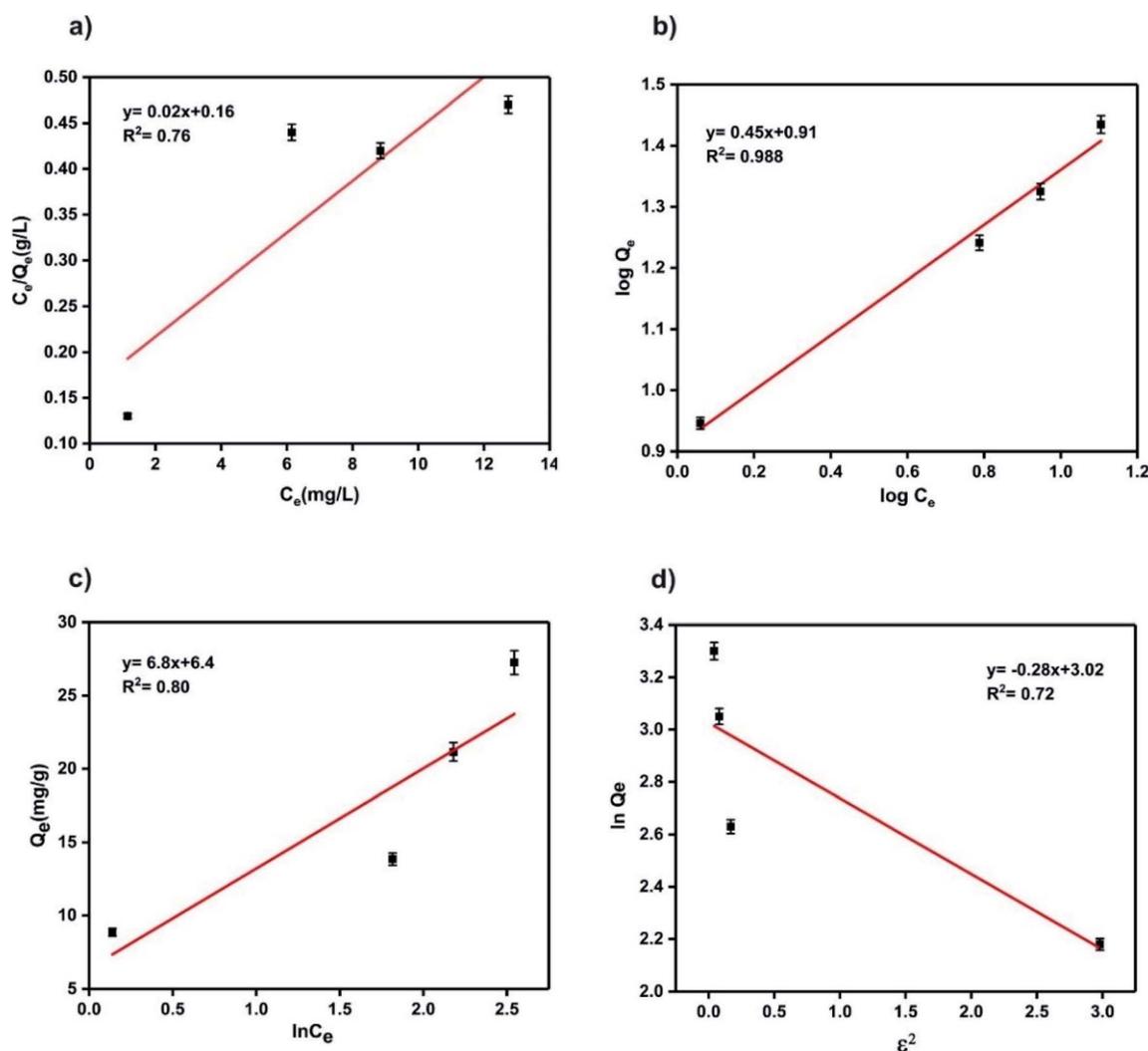
$$R_L = 1/(1 + K_L C_0) \quad (9)$$

Fig. 15 Langmuir (a), Freundlich (b), Temkin (c) and (D–R) (d) isotherm plots for dye adsorption of ternary NC.

In which C_e is the equilibrium concentration of adsorbate in solution (mg L^{-1}), q_e denotes the amount of dye adsorbed in equilibrium (mg g^{-1}), Q_m represents the maximum adsorption capacity, K_L is the Langmuir constant (L mg^{-1}) which can be obtained by plotting C_e/q_e versus C_e. The basic features of Langmuir adsorption can be determined by R_L, which demonstrates the ability of the adsorbent to separate contaminants. The lower the amount of R_L, the better the adsorption on the adsorbent. $R_L > 1$ indicates unfavorable adsorption, while $R_L = 1$, $0 < R_L < 1$, and $R_L = 0$ represent linear, favorable, and irreversible adsorption processes. According to Fig. 15(a) and Table 5, the maximum adsorption capacity of the adsorbent determined by the Langmuir model was $Q_{m,call} = 35.7$ mg g^{-1}, and R_L was 0.2, implying favorable adsorption.

The Freundlich isotherm describes multilayer surface adsorption on a heterogeneous adsorbent surface with non-uniform heat distribution. The heterogeneous surface implies the presence of different types of bonds or active adsorption sites such as carboxyl, hydroxyl, and amine on the surface.[62] The Freundlich isotherm assumes that stronger junctions are first occupied; the strength of the junction decreases with the occupation of the site.[63] The linear form of this model has the following form:

$$\mathrm{Ln}\ q_e = \ln K_F + (1/n) \ln C_e \tag{10}$$

where K_F (L g^{-1}) and $1/n$ can be obtained from the slope and the interception of the plot of ln q_e versus ln C_e, respectively. The Freundlich coefficient (n), related to the adsorption intensity, must be in the range of 1 to 10 for desirable adsorption. Based on Fig. 15(b) and Table 5, this value was $n = 2.22$, so the MG adsorption on the NC is desirable.

Temkin isotherm also addresses the adsorbent–adsorbate interaction. In this model, the adsorption process is determined by the uniform distribution of the bonding energy at the adsorbent surface. It is assumed that the heat of adsorption is not constant and decreases with increasing adsorption surface coverage due to the adsorbent–adsorbate interactions.[64] In this model, free adsorption energy is a function of surface coverage.[65] The linear form of Temkin isotherm can be expressed by:

$$Q_e = B \ln K_T + B \ln C_e \tag{11}$$

$$B = RT/b_T \tag{12}$$

where R is the universal gas constant (8.3 J mol^{-1} K^{-1}), T shows the temperature (K), K_T denotes the equilibrium binding constant (L g^{-1}), B is a dimensionless constant related to the heat of adsorption, and b_T (kJ mol^{-1}) is an indicator of the adsorption ability of the adsorbent. B and K_T can be determined by plotting Q_e versus ln C_e, as shown in Fig. 15(c). According to Table 5, B, K_T, b_T, and R^2 are 6.8, 2.6 L g^{-1}, 3.63 kJ mol^{-1}, and 0.8, respectively.

The D–R isotherm model investigated the adsorption mechanism on both heterogeneous and homogeneous surfaces.[66] Also, it is an experimental model to describe the mechanism of filling adsorbent pores. The linear D–R isotherm was represented in eqn (13):

$$\mathrm{Ln}\ Q_e = \ln Q_m - K_{DR}\varepsilon^2 \tag{13}$$

$$\varepsilon = RT \ln(1 + 1/C_e) \tag{14}$$

$$E = (1/2K_{DR})^{1/2} \tag{15}$$

where Q_e shows the amount of adsorbate material adsorbed per unit mass of adsorbent at equilibrium, Q_m is the maximum adsorption capacity, K_{DR} denotes a constant related to adsorption energy, and ε is adsorption potential. The parameter of K_{DR} can be obtained by plotting ln Q_e vs. ε^2, while the mean free energy, E (kJ mol^{-1}), can be calculated by eqn (15) to determine the type of adsorption. For $E < 8$ kJ mol^{-1}, physisorption governs the reaction, while $8 < E < 16$ kJ mol^{-1} indicates chemisorption. Due to the low regression coefficient ($R^2 = 0.72$), the adsorption of MG by polymeric NC is not consistent with this model.[67] The sequence of regression coefficient of the four isotherm models:
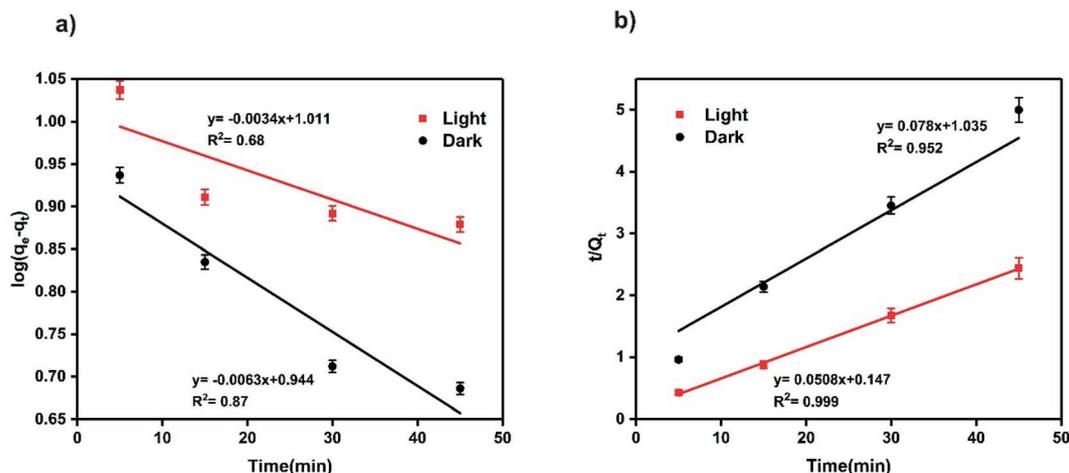

Fig. 16 (a) pseudo-first-order kinetic (b) pseudo-second-order kinetic of MG removal by ternary NC.

Table 5 Calculated parameters from several adsorption isotherm models for the adsorption of MG on ternary NC

Freundlich		Langmuir		Temkin		(D–R)	
n	2.22	Q_m (mg g^{-1})	35.7	B	6.8	K_{DR} (mol^2 kJ^{-2})	0.28
K_F (L g^{-1})	8.130	K_L (L mg^{-1})	0.18	K_T (L g^{-1})	2.6	q_m (mg g^{-1})	20.49
		R_L	0.2	b_T (kJ mol^{-1})	3.63	E (kJ mol^{-1})	1.3
R^2	0.988	R^2	0.76	R^2	0.80	R^2	0.72

$R_{Frendlich}^2 = 0.988 > R_{Temkin}^2 = 0.80 > R_{Longmuyer}^2 = 0.76 > R_{D-R}^2 = 0.72$, clear that the correlation coefficient of the Freundlich model was much higher than the three other isotherms. It can be concluded that the adsorption of MG by ternary NC follows the Freundlich isotherm, which is consistent with the hetero-structure of the prepared ternary NC. Furthermore, the second rank isotherm in the correlation coefficient order was the Temkin model confirming the non-uniform surface coverage of the adsorbent, which is expected in the heterogenous NC sorbent.

3.8.6. Kinetics of removal process. A quantitative perception of adsorption and the rate of adsorption on the solid–liquid interface can be achieved by kinetic models. Removal (adsorption/degradation) reaction constants can be calculated using the Lagergren equation (pseudo-first-order) and the Hu equation (pseudo-second-order).[68] The reaction time was varied while all other parameters were kept constant to explore reaction kinetics. The pseudo-first-order (PFO) equation associates the adsorption rate of occupation sites with non-occupied sites.[69] Moreover, it suggests the monolayered kinetics of diffusion. In this model, q_e and q_t demonstrate the amount (mg g^{-1}) of removed dye in equilibrium and at the time of t (min), respectively. The PFO rate constant (k_1 in min^{-1}) shows the reaction speed, which can be obtained by the plot of $\log(q_e - q_t)$ versus t as follows:

$$\text{Log}(q_e - q_t) = \log q_e - k_1 t/2.303 \tag{16}$$

The plot of PFO kinetics of dye removal is shown in Fig. 16(a), and corresponding derived parameters are exhibited in Table 6.

The pseudo-second-order (PSO) kinetics assumes that chemical adsorption controls the interactions. In adsorption processes, changing the concentration of a reactant or product per unit time determines the reaction rate in a chemical process.[69] Eqn (17) states PSO kinetics of reactions, in which k_2 is the second-order rate constant (g mg^{-1} min^{-1}).

$$t/q_t = 1/k_2 q_e^2 + t/q_e \tag{17}$$

The linear plot of t/q_t versus t is depicted in Fig. 16(b), and the corresponding derived parameters are exhibited in Table 6. As seen in this table, the correlation coefficient of PSO model is much higher than that of the PFO model (both for dark and light conditions), so it can be concluded that the removal process of MG by the synthesized ternary NC predominantly followed the PSO kinetic model, suggesting the dependence of adsorption and removal on the amount of solutes adsorbed on

the adsorbent surface as well as the number of active sites. It can be said that dye removal by the NC is mainly due to chemisorption and electron transfer capability.[70,71]

3.8.7. Catalyst regeneration test. From an environmental and economic point of view, one of the most critical issues in adsorbing and removing contaminants by the catalyst is its regeneration and reuse. In this regard, 0.1 g of the synthesized NC has been dispersed in 50 mL of MG solution (20 PPM; pH = 7) and stirred for 15 min at room temperature. The residual dye concentration has been determined by a UV-visible spectrophotometer. The catalyst was then removed from the solution and stirred with 50 mL HCl (0.1 M) for 10 min and rinsed with a mixture of water and ethanol several times and used again under the previous conditions to remove the dye. This process was repeated in 5 cycles. Fig. 17 shows the percentage of dye

Table 6 Parameter of kinetics models for removal of MG using ternary NC under light and dark conditions

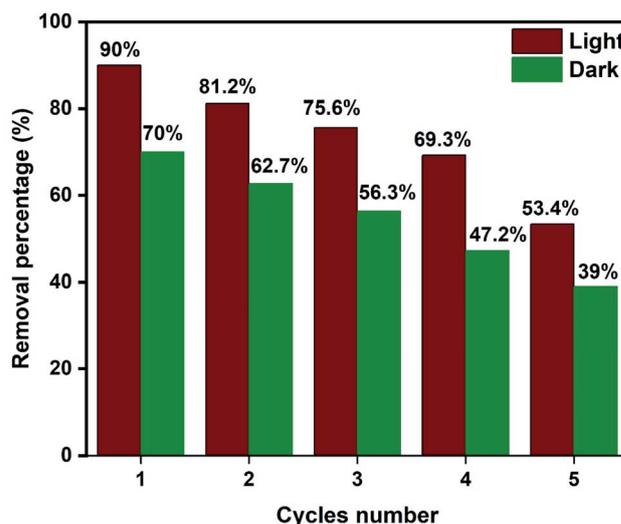|	Pseudo-first order			Pseudo-second order	
	Light	Dark		Light	Dark
$Q_{e,cal}$ (mg g^{-1})	10.28	8.8	$Q_{e,exp}$ (mg g^{-1})	17.2	13.85
K_1 (min^{-1})	0.008	0.015	$Q_{e,cal}$ (mg g^{-1})	19.69	12.82
R^2	0.68	0.87	K_2 (g mg^{-1} min^{-1})	0.018	0.0058
			R^2	0.999	0.952

Fig. 17 Reusing plot of the NC in light and dark conditions at 5 cycles.

removal by the catalyst in dark and light conditions in 5 cycles. As shown in the diagram, the catalyst can be regenerated and reused well.

3.8.8. Mechanism of adsorption. The interactions between the ZnS@GO@Pani NC and the MG dye during the adsorption process are schematically illustrated in Fig. 18. The accumulation of a substance at the liquid–solid or gas–solid interface is called the adsorption process. The adsorption is usually defined by interactions such as hydrogen bonding, coordination bonding, ionic bonding, and π–π interactions. Electrostatic attraction is formed between the positively charged ammonium group of MG dye and the negatively charged adsorbent sites such as the carboxyl group of GO and the sulfonate group of the dopant. Moreover, hydrogen bonding between the amine group of MG and the (–NH) groups of Pani and OH groups of GO is another interaction involved in the adsorption process. Furthermore, the adsorption mechanism can also be enhanced through the π–π stacking interaction of conjugated MG molecules and the aromatic skeleton of the GO@Pani NC.[11,50,60]

3.8.9. Mechanism of photocatalytic degradation of MG. The energy band structure of ternary NC must be studied to understand the charge transfer processes and probable redox reaction pathways involved in the photocatalytic degradation of MG. Regarding previous reports, Pani has been known as a p-type semiconductor with the lowest unoccupied molecular orbital energy (E_{LUMO}) of −1.9 eV (relative to standard hydrogen electrode potential; NHE) and the highest occupied molecular orbital (E_{HOMO}) energy of 0.8 eV (versus NHE), resulting in an energy gap of 2.7 eV.[50,72] GO is a p-type semiconductor whose conduction and valence band edges (CB and VB, respectively) lay in $E_{CB} = -0.75$ and $E_{VB} = 2.05$ eV (versus NHE), giving rise to an energy gap of 2.8 eV. Finally, ZnS is an n-type semiconductor with a wide energy gap of 3.56 eV due to the configuration of its band edges ($E_{CB} = -1.07$, $E_{VB} = 2.49$ eV; versus NHE).[73,74] Fig. 19 shows the energy band structures of these materials versus NHE potential before and after contact. The Fermi level for the n-type semiconductor is near its CB edge, while that of the p-type one lies near the VB edge. A p–n–p heterojunction is formed upon
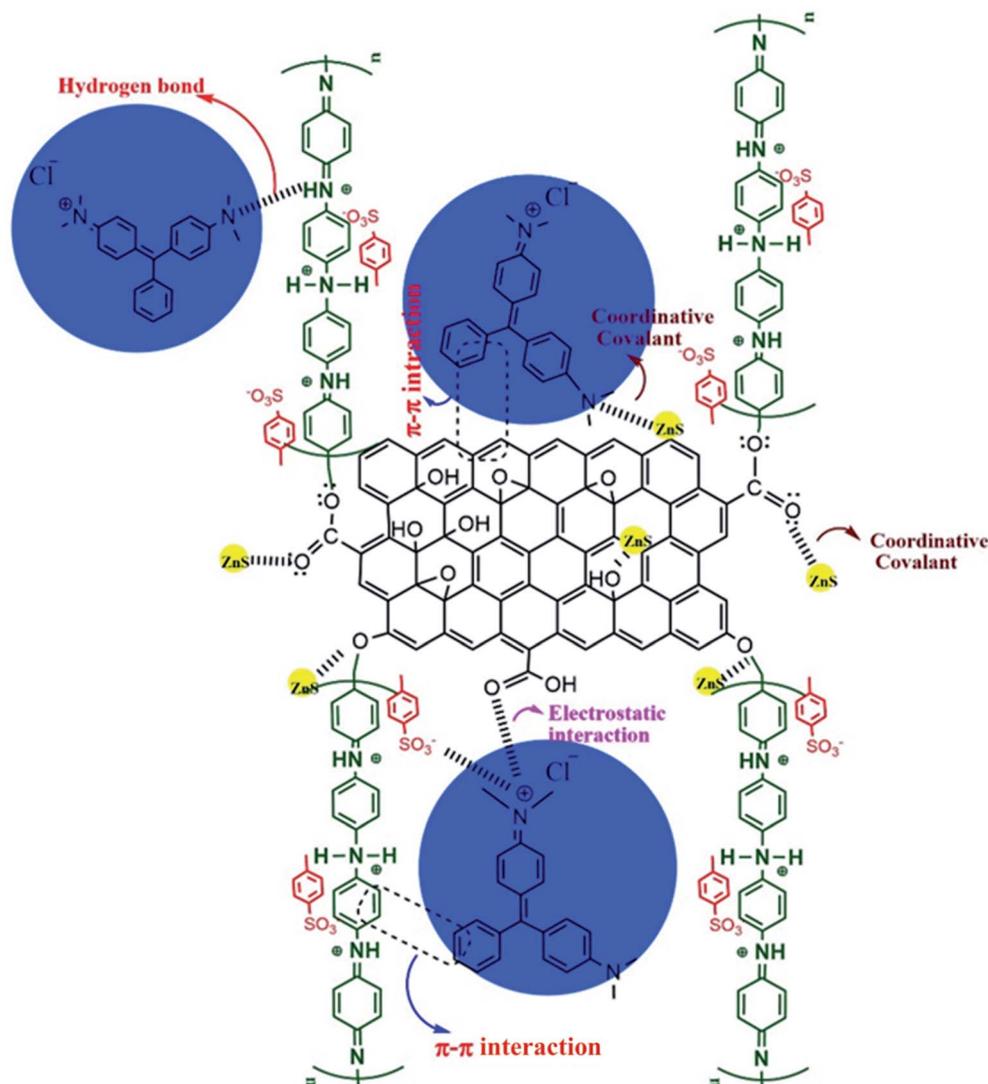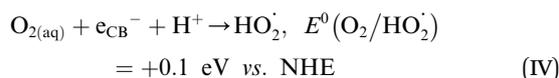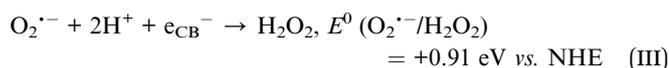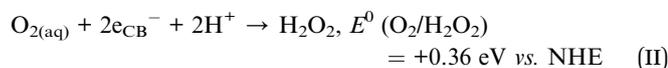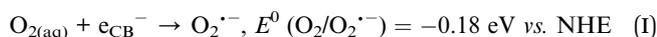

Fig. 18 The interaction between the Pani@GO@ZnS NC and the MG dye molecule during the adsorption process.
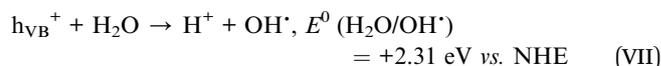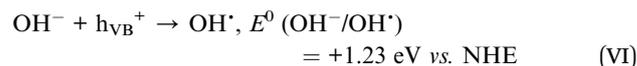
the combination of these compounds. The transfer of the electrons from ZnS Fermi level to GO and Pani Fermi levels leads to an equilibrium Fermi level.[48,75–77] Furthermore, this electron transfer resulted in displacement and bending of both valence and conduction bands of the three counterparts of the ternary NC. Although the energy bands of ZnS and GO are nested before contact, after forming NCs, the whole ZnS energy band shifts downward. In contrast, the GO energy bands move upward, resulting in a new energy band arrangement between these two semiconductors. Moreover, the HOMO and LUMO of Pani partly shift upward. Due to the electron transfer and the formation of p–n–p junction at the interfaces of ZnS, GO, and Pani, an internal electric field is formed in each binary p–n junction, which can effectively separate the photoinduced electron–hole pairs. The presence of an internal electric field increases the transfer rate of the electron–hole carriers and prevents their recombination, which improves the photocatalytic efficiency of the ternary NC.[48,76–79] Therefore, it can be said that this NC is composed of double type II heterogeneous photocatalysts.[29,30,79] Upon exposure to natural light, all three components are excited, giving rise to the accumulation of electrons and holes at the CB and VB of each case, respectively. Electrons are injected from the LUMO of Pani and the CB of GO into the CB of ZnS because the CB edge of the ZnS is more positive than the LUMO of Pani and CB of GO. Furthermore, the photoinduced holes migrate from the VB of ZnS to the VB of GO and Pani. The final position of the energy bands of the composite components limits the pathways for the production of active radicals due to the interaction of photoexcited electron–holes with the environment. The edge of the CB of ZnS NPs in the composite, *i.e.*, the level of accumulation of electrons, has sufficient reduction potential to produce superoxide radical ions $(O_2^{\bullet-})$ and hydrogen peroxide (H_2O_2). The molecular oxygen dissolved in MG solution is adsorbed on the surface of the composite and ZnS NPs. It reacts with the electrons in the CB of ZnS, causing single, double, or multiple electron reduction of molecular oxygen. The single electron O_2 reduction leads to the formation of superoxide radicals, whereas the two-electron O_2 reduction results in hydrogen peroxide production. Also, superoxide union can be further reduced to form hydrogen peroxide:[80–82]

$$O_{2(aq)} + e_{CB}^- \rightarrow O_2^{\bullet-}, \; E^0 \, (O_2/O_2^{\bullet-}) = -0.18 \text{ eV } vs. \text{ NHE} \quad \text{(I)}$$

$$O_{2(aq)} + 2e_{CB}^- + 2H^+ \rightarrow H_2O_2, \; E^0 \, (O_2/H_2O_2)$$
$$= +0.36 \text{ eV } vs. \text{ NHE} \quad \text{(II)}$$

$$O_2^{\bullet-} + 2H^+ + e_{CB}^- \rightarrow H_2O_2, \; E^0 \, (O_2^{\bullet-}/H_2O_2)$$
$$= +0.91 \text{ eV } vs. \text{ NHE} \quad \text{(III)}$$

$$O_{2(aq)} + e_{CB}^- + H^+ \rightarrow HO_2^{\bullet}, \; E^0 \, (O_2/HO_2^{\bullet})$$
$$= +0.1 \text{ eV } vs. \text{ NHE} \quad \text{(IV)}$$

(H_2O_2) can be further reduced and form hydroxyl radicals:

$$H_2O_2 + H^+ + e_{CB}^- \rightarrow H_2O + OH^{\bullet}, \; E^0 \, (H_2O_2/OH^{\bullet})$$
$$= +0.39 \text{ eV } vs. \text{ NHE} \quad \text{(V)}$$
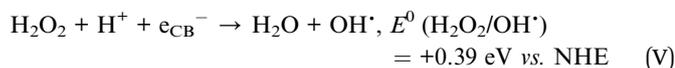
These active species $(OH^{\bullet}, HO_2^{\bullet}, H_2O_2, O_2^{\bullet-})$ react with and decompose the dye molecule. Due to the final position of the energy bands of ternary NC components, oxidation of water or hydroxyl ions induced by the interaction of the holes accumulated on VB of GO or HOMO of Pani with water or hydroxyl ions that are adsorbed on the surface alternative pathways for the production of strong oxidizing agent $OH^{\bullet}$ (hydroxyl radical) is not possible. This impossibility refers to the fact that the oxidation potential of these reactions is more positive than the mentioned levels:[80]

$$OH^- + h_{VB}^+ \rightarrow OH^{\bullet}, \; E^0 \, (OH^-/OH^{\bullet})$$
$$= +1.23 \text{ eV } vs. \text{ NHE} \quad \text{(VI)}$$

$$h_{VB}^+ + H_2O \rightarrow H^+ + OH^{\bullet}, \; E^0 \, (H_2O/OH^{\bullet})$$
$$= +2.31 \text{ eV } vs. \text{ NHE} \quad \text{(VII)}$$

It should be noted that the electrons of CB (e_{CB}) and holes of VB (h_{VB}) can directly react with surface-adsorbed dye molecule, oxidizing/reducing it to unstable ion, resulting in dye decomposition.[82,83] Another pathway for the decomposition of MG dye involves a dye-photosensitization mechanism in which MG is photoexcited, transferring electrons from the HOMO level of dye to its LUMO. The electron in LUMO level or hole in the HOMO level of dye can be transferred to CB or VB of NP photocatalyst, respectively. Injected e^-/h^+ can subsequently trigger the reactions to form radical species, further decomposing the unstable dye ions. Such a mechanism has been studied in other reports.[12,83,84] It is worth noting that the ability of high dye adsorption by the ternary NC can increase the local condensation of dye molecules around the photocatalytic particle compared to the dye concentration in the whole solution. This increases the probability of these molecules being targeted by the reactive oxygen species (ROS), which will positively affect the decolorization of the dye in the aqueous solution, implying the synergetic effect of adsorption–photocatalytic degradation mechanisms of dye removal.[82,83,85]

As a final remark, it is noteworthy to address the role of hydrogen bonding in the photocatalytic degradation of MG dye by the prepared ternary NC. At first, hydrogen bonding participates in the adsorption of MG dye on the NC surface, which causes the reaction of visible light-induced charges and ROS formed on the NC surface with the dye molecule, destroying its structure and turning it into other compounds. In addition, the presence of hydrogen bonds facilitates some bond breaking, such as N–C and N–H, by relying on the idea that it strengthens by the back-donation.[86] Also, since the reaction takes place in an aqueous medium, the photocatalytic effect can cause the breakdown of water into active species, including hydrogen and hydroxyl radicals, which effectively decompose MG. In this way, after binding to the surface of the NC with hydrogen bonds, a water molecule can break upon UV harvesting into hydrogen and hydroxyl radicals more efficiently.[86] It is also reported that a hydrogen bond-based heterojunction photocatalyst (composed of two organic components) can be considered an efficient structure for photoinduced electron/hole transfer and suppressing their recombination. In this structure, an inner
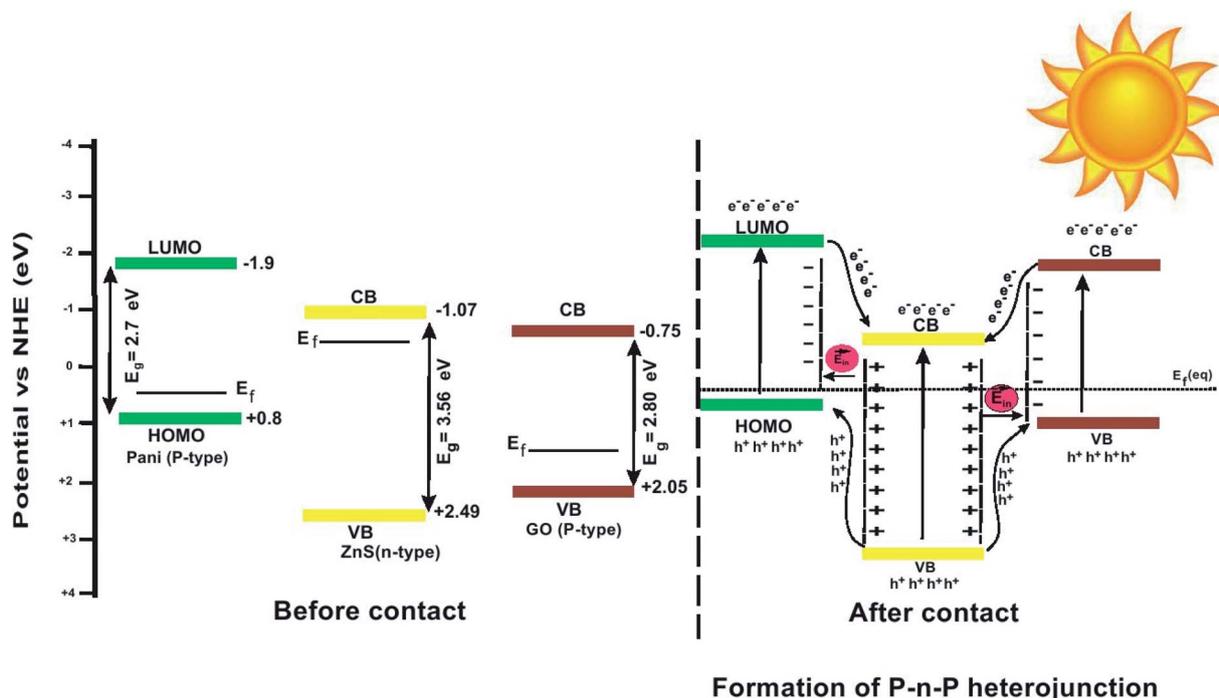
Fig. 19 Possible charge transfer pathways for photocatalytic degradation of MG in the presence of ternary NC.

Table 7 Comparison between removal efficiency of synthesized ternary NC and other reported NC in literature

Nanocomposite	Dye	Con. of dye $(mg\ L^{-1})$	Dosage of catalyst $(mg\ mL^{-1})$	Time (min)	Efficiency%	Irradiation source	Mechanism of removal	Reference
PANI/GO	MB	50	—	270	86	—	Adsorption	88
PANI/RGO					91			
Chitosan/PANI/Co$_3$O$_4$	MB	10	0.3	180	88	UV	Degradation	89
CNT/PANI	MG	16	1	120	88	UV	Degradation	90
PANI/SrTiO$_3$	MB	10	0.3	90	97	Visible	Degradation	91
PANI/ZnO	MB	10	0.25	300	97	Natural sunlight	Degradation	92
	MG				99			
ZnO/RGO/PANI	MO	10	0.5	60	100	UV	Degradation	93
Graphene/PANI	RB	—	—	180	56	Visible	Degradation	94
Geraphene/PANI/CuO	CR	10	0.5	20	97.91	UV	Degradation	95
PEO/PANI	MO	5	2.5	50	99	—	Adsorption	96
PANI/CdS	MB	20	0.5	300	92	Visible	Degradation	97
g-AP–PPA/TiO$_2$–Au	MV	20	1.25	240	92	Sunlight	Adsorption & degradation	98
ZnS@GO@PANI	MG	20	2	15	90	Natural light dark	Adsorption & degradation	Present work
				15	70			

electric field between the two ends of the hydrogen bond is created before light irradiation. When light is applied, the NC is excited to form electron–hole pairs, which are efficiently separated by the inner electric field. Actually, hydrogen bonding creates an ultrafast pathway; not only the hydrogen bonds are shorter than van der Waals junctions but also the inner electric field formed between the two ends of the hydrogen bonds.[87] Such a mechanism may take place in the prepared ternary NC through H bonding between the Pani and GO components or between the adsorbed dye and the NC.

Table 7 summarizes different dyes' experimental parameters and removal efficiency using some reported nanocomposites. Accordingly, the prepared ternary NC exhibited a rapid and high-efficiency MG removal in darkness and under natural light.

3.9. Antibacterial activity

The antibacterial activity of synthesized GO@Pani and ZnS@GO@Pani NCs was tested against Gram-negative (*E. coli*, *P. aeruginosa*) and Gram-positive (*S. aureus*, *B. subtilis*) bacteria. Fig. 20 shows the inhibition zone of bacteria formed by the NCs
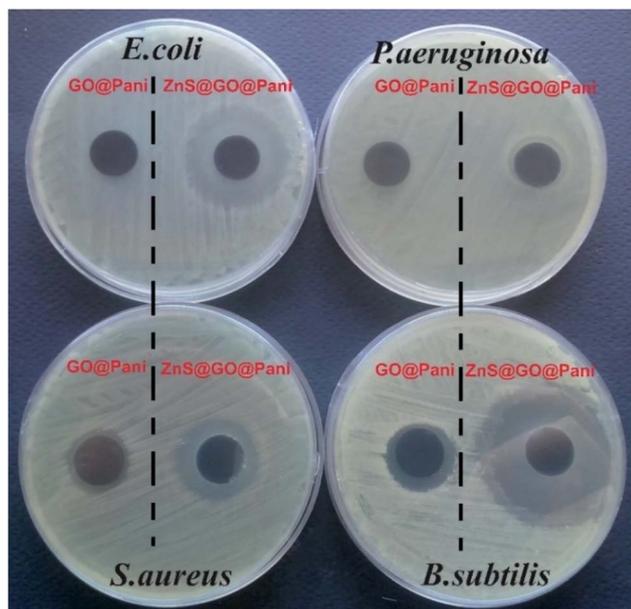
Fig. 20 Zones of inhibition exhibited by GO@Pani and ZnS@GO@Pani NCs against *E. coli P. aeruginosa, S. aureus*, and *B. subtilis* bacteria.

Table 9 Antibacterial activity of some Pani-based nanoparticles against studied bacteria reported in previous papers

Nanocomposite	Inhibition zone (mm)	Reference
Pani/Cu–ZnO	*E. coli* (33.8)	107
	S. aureus (36.4)	
GO–Pani	*E. coli* (22)	108
	S. aureus (18.5)	
Pani–Au	*E. coli* (25)	109
	S. aureus (24)	
Pani–Ag–Au	*E. coli* (29)	109
	S. aureus (31)	
Pure Pani	*E. coli* (10)	110
	S. aureus (11)	
Ag–Pani–rGO	*E. coli* (16)	111
	S. aureus (23)	
	P. aeruginosa (12)	
	B. subtilis (17)	
ZnS@GO@Pani	*E. coli* (29.0 ± 1.4)	Present work
	S. aureus (21.5 ± 0.7)	
	P. aeruginosa (15.5 ± 0.7)	
	B. subtilis (37.0 ± 1.4)	

under the light. The diameter of the zone of inhibition (ZOI) against various bacteria is listed in Table 8. As can be seen, the GO@Pani NC showed an acceptable antibacterial activity against Gram-positive (*S. aureus*, *B. subtilis*) bacteria. However, the ternary NC exhibited excellent ZOI against both Gram-positive and Gram-negative bacteria, comparable to the antibacterial activity of two well-known antibiotics of gentamicin and chloramphenicol. The antibacterial activity of some reported nanomaterials is also summarized in Table 9, further confirming the superior antibacterial activity of the prepared ternary NC. In our previous study, the effect of ZnS NPs on *S. aureus* and *E. coli* bacteria was investigated, which revealed the resistance of *E. coli* bacteria.[32] In comparison, it seems that the hybrid of ultrafine ZnS NPs with GO@Pani nanocomposite led to an excellent synergistic effect. The zinc ions present in the NC can deactivate the bacteria by easy release, anchor to the cell wall, and reaction with thiol groups of the vital enzymes of bacteria. Besides, the presence of these ions denatures the proteins and impairs the ability of DNA to reproduce, thus leading to the death of the pathogen.[99–101] The photocatalytic

activity of ternary NC can also generate ROS species such as hydrogen peroxide, superoxide, and electrons.[102] The reactive superoxide and electrons can adhere to the cell surface due to their negative charge, and hydrogen peroxide can pass through the cell membrane.[47] On the other hand, the antibacterial properties of polyaniline can be due to ROS species like H_2O_2, which leads to oxidative stress, oxidation of amino acids in proteins, and damage to the DNA and lipids. Besides, Pani NPs doped with *p*-TSA possess NH^+ surface groups, inhibiting the growth and nutrition of bacteria and destabilizing the cytoplasmic membrane due to electrostatic interactions between Pani and negative sides of bacteria.[103–105] Upon contact, GO can also cause bacterial death through physical interactions such as membrane damage by sharp edges and oxidative stress *via* chemical interactions that oxidize proteins, fats, and nucleic acids.[106] Numerous studies have reported higher resistance of Gram-negative bacteria toward nanomaterials due to their impermeable wall and the presence of lipopolysaccharides in their outer membrane.[47] Interestingly, the synthesized ternary NC showed strong antibacterial activity even against Gram-negative bacteria.

Table 8 Antibacterial activity of GO@Pani and ZnS@GO@Pani NCs using Kirby–Bauer technique

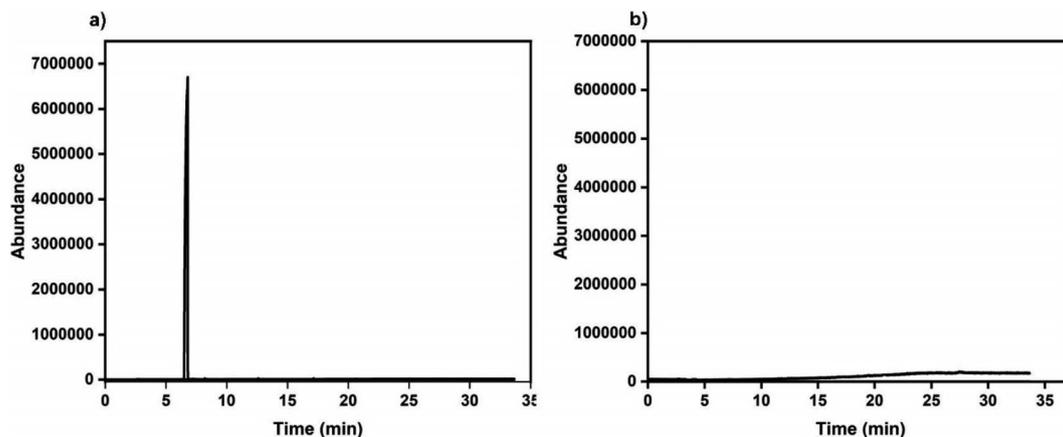| Test strain	Zone of growth inhibition (mm)			
	Pani@GO	Pani@GO@ZnS	Gentamicin (10 µg per disc)	Chloramphenicol (30 µg per disc)
E. coli	NE	29.0 ± 1.4	19.6 ± 1.1	20.7 ± 1.5
P. aeruginosa	NE	15.5 ± 0.7	15.6 ± 0.5	NE[a]
S. aureus	14.5 ± 0.7	21.5 ± 0.7	20.3 ± 1.5	21.7 ± 0.6
B. subtilis	17.5 ± 0.7	37.0 ± 1.4	26.0 ± 1.7	22.3 ± 1.2

[a] No effect.

Fig. 21 GC-MS spectrum of (a) pure aniline and (b) remaining solution treated by the prepared ternary NC.

3.10. Leaching study

Zinc is one of the essential elements for humans and aquatic animals, but its excessive consumption causes poisoning. For this purpose, atomic absorption analysis evaluated the amount of zinc ion leaching in an aqueous solution. 0.1 g of the NC was dispersed in 50 mL MG solution (20 ppm, pH = 7, room temperature) and stirred for 15 min. The catalyst was then removed, and the remaining solution was used for atomic absorption analysis. The amount of zinc ion was determined to be 0.028 $\mu g \ L^{-1}$, which was within the acceptable range of the World Health Organization (WHO).[112,113] Since aniline is a highly toxic monomer, GC-MS analysis was used to explore whether the monomer remained in the composite structure. For comparison, some aniline was first dissolved in ethanol, and the GC-MS spectrum was investigated. As shown in Fig. 21(a), the aniline peak appears in $t = 6$ min. In the next step, 0.1 g NC was dispersed in 50 mL ethanol and stirred for 15 min, and after removing the catalyst, the GC spectrum of the remaining solution was examined. If unpolymerized aniline were present in the NC structure, it would dissolve in ethanol and could be detected by GC-MS analysis. As shown in the relevant spectrum (Fig. 21(b)), there is no trace of aniline, confirming that the prepared ternary NC can be used as a safe and non-toxic dye removal agent.

4. Conclusion

Using a facile wet chemical method, a ternary NC was synthesized based on polyaniline, graphene oxide, zinc sulfide; (ZnS@GO@Pani). The ultrafine mono-dispersed ZnS NPs with an average size of 5 nm were uniformly distributed and grafted to the GO@Pani matrix. The ZnS particles are crystallized in a FCC phase structure with an average lattice parameter of $a_0 = 5.3080$ Å. The synthesized ternary NC is a visible light photo-active material with a bandgap energy of 2.72 eV. The TGA analysis of both binary and ternary NCs shows a three-step weight loss from room temperature to 600 °C with high char yields of 60.7% and 70.1% for GO@Pani and ZnS@GO@Pani NCs, respectively, implying considerable thermal stability of

these NCs. It was observed that the dosage of 2 mg mL^{-1} of the mesoporous ternary NC in 20 ppm aqueous MG solution results in 70% and 90% efficiency of the dye removal within 15 min in darkness and under natural light, respectively. The dye removal in darkness solely corresponded to adsorption, while the integrated photocatalysis–adsorption mechanism was involved in the dye removal activity under the light. The present research reported, for the first time, an effective sorbent that can simultaneously act as a type II p–n–p heterojunction photocatalyst for the rapid and efficient removal of risky organic pollutants. The adsorption data were well-matched with the Freundlich isotherm model indicating multilayer adsorption on the heterogeneous surface of the ternary NC. The kinetics of the dye removal showed an excellent consistency with the pseudo-second-order model, confirming the chemisorption of MG due to the presence of functional groups in the NC and hydrogen bonding. Additionally, electrostatic interaction and π–π stacking can lead to the physisorption of MG by the NC, promoting a beneficial role in the dye removal process. Antibacterial tests revealed the superior antibacterial activity of ZnS@GO@Pani NC against both Gram-negative (*E. coli*, *P. aeruginosa*) and Gram-positive (*S. aureus*, *B. subtilis*) bacteria. The leaching and regeneration studies also confirmed that the prepared NC is a non-toxic dye removal agent with good reusability.

Conflicts of interest

There are no conflicts of interest to declare.

References

1 Y. Chen, Z. Xiang, D. Wang, J. Kang and H. Qi, *RSC Adv.*, 2020, **10**, 23936–23943.

2 W. Liu, T. He, Y. Wang, G. Ning, Z. Xu, X. Chen, X. Hu, Y. Wu and Y. Zhao, *Sci. Rep.*, 2020, **10**, 1–12.

3 J. G. McEvoy and Z. Zhang, *J. Photochem. Photobiol., A*, 2016, **321**, 161–170.

4 S. Bera, M. Pal, A. Naskar and S. Jana, *J. Alloys Compd.*, 2016, **669**, 177–186.

5 S. Balakumar, V. Keller and M. Shankar, *Nanostructured Materials for Environmental Applications*, Springer, 2021.

6 S. Dutta, B. Gupta, S. K. Srivastava and A. K. Gupta, *Mater. Adv.*, 2021, **2**, 4497–4531.

7 K. Karthik, A. Raghu, K. R. Reddy, R. Ravishankar, M. Sangeeta, N. P. Shetti and C. V. Reddy, *Chemosphere*, 2022, **287**, 132081.

8 K. Kannan, D. Radhika, K. K. Sadasivuni, K. R. Reddy and A. V. Raghu, *Adv. Colloid Interface Sci.*, 2020, **281**, 102178.

9 K. R. Reddy, M. Jyothi, A. Raghu, V. Sadhu, S. Naveen and T. M. Aminabhavi, in *Nanophotocatalysis and Environmental Applications*, Springer, 2020, pp. 139–169.

10 K. Rokesh, M. Sakar and T.-O. Do, *Nanomaterials*, 2021, **11**, 572.

11 A. B. Djurišić, Y. He and A. M. Ng, *APL Mater.*, 2020, **8**, 030903.

12 M. Mitra, S. T. Ahamed, A. Ghosh, A. Mondal, K. Kargupta, S. Ganguly and D. Banerjee, *ACS Omega*, 2019, **4**, 1623–1635.

13 N. V. Nerkar, S. B. Kondawar, S. K. Brahme and Y. H. Kim, *Int. J. Mod. Phys. B*, 2018, **32**, 1840085.

14 A. Muhammad, A.-u.-H. A. Shah, S. Bilal and G. Rahman, *Materials*, 2019, **12**, 1764.

15 S. Sharma, S. Singh and N. Khare, *Colloid Polym. Sci.*, 2016, **294**, 917–926.

16 F. Chen, Y. Cao and D. Jia, *Ceram. Int.*, 2015, **41**, 6645–6652.

17 X. Chen, H. Li, M. Chen, W. Li, Z. Yuan and R. Snyders, *Mater. Chem. Phys.*, 2019, **227**, 368–374.

18 N. A. Al-Rawashdeh, O. Allabadi and M. T. Aljarrah, *ACS Omega*, 2020, **5**, 28046–28055.

19 S. Ibrahim, S. Chakrabarty, S. Ghosh and T. Pal, *ChemistrySelect*, 2017, **2**, 537–545.

20 J. Patel, A. K. Singh and S. Carabineiro, *Nanomaterials*, 2020, **10**, 964.

21 H.-Y. Jing, T. Wen, C.-M. Fan, G.-Q. Gao, S.-L. Zhong and A.-W. Xu, *J. Mater. Chem. A*, 2014, **2**, 14563–14570.

22 H. Atout, A. Bouguettoucha, D. Chebli, J. Gatica, H. Vidal, M. P. Yeste and A. Amrane, *Arabian J. Sci. Eng.*, 2017, **42**, 1475–1486.

23 N. Yahya, F. Aziz, N. Jamaludin, M. Mutalib, A. Ismail, W. Salleh, J. Jaafar, N. Yusof and N. Ludin, *J. Environ. Chem. Eng.*, 2018, **6**, 7411–7425.

24 O. S. Ekande and M. Kumar, *J. Environ. Chem. Eng.*, 2021, **9**, 105725.

25 D.-T. Phan and G.-S. Chung, *J. Phys. Chem. Solids*, 2013, **74**, 1509–1514.

26 T.-F. Yeh, J. Cihlář, C.-Y. Chang, C. Cheng and H. Teng, *Mater. Today*, 2013, **16**, 78–84.

27 M. A. Khan, R. Govindasamy, A. Ahmad, M. R. Siddiqui, S. A. Alshareef, A. A. H. Hakami and M. Rafatullah, *Polymers*, 2021, **13**, 419.

28 H. Wang, M. Duan, Y. Guo, C. Wang, Z. Shi, J. Liu and J. Lv, *Water Sci. Technol.*, 2018, **77**, 2751–2760.

29 X. Hong, X. Wang, Y. Li, J. Fu and B. Liang, *Catalysts*, 2020, **10**, 921.

30 K. Sridharan, S. Shenoy, S. G. Kumar, C. Terashima, A. Fujishima and S. Pitchaimuthu, *Catalysts*, 2021, **11**, 426.

31 H. Kim and B. L. Yang, *New J. Chem.*, 2019, **43**, 16699–16705.

32 H. Bagheri, M. A. Pasha and M. M. Lakouraj, *Phys. Scr.*, 2020, **95**, 095703.

33 R. Karthik and S. Thambidurai, *J. Mater. Sci.: Mater. Electron.*, 2017, **28**, 9836–9851.

34 B. Butoi, A. Groza, P. Dinca, A. Balan and V. Barna, *Polymers*, 2017, **9**, 732.

35 Y. Zhang, J. Liu, Y. Zhang, J. Liu and Y. Duan, *RSC Adv.*, 2017, **7**, 54031–54038.

36 M. Das and D. Sarkar, *Ceram. Int.*, 2017, **43**, 11123–11131.

37 L. R. Vargas, A. K. Poli, R. d. C. L. Dutra, C. B. d. Souza, M. R. Baldan and E. S. Gonçalves, *J. Aerosp. Technol. Manage.*, 2017, **9**, 29–38.

38 H. Kweon, C.-W. Lin, M. F. Hasan, R. Kaner and G. N. Sant, *ACS Appl. Polym. Mater.*, 2019, **1**, 3233–3241.

39 M. Acik, C. Mattevi, C. Gong, G. Lee, K. Cho, M. Chhowalla and Y. J. Chabal, *ACS Nano*, 2010, **4**, 5861–5868.

40 G. Gaikwad, P. Patil, D. Patil and J. Naik, *Mater. Sci. Eng., B*, 2017, **218**, 14–22.

41 S. Konwer, *J. Mater. Sci.: Mater. Electron.*, 2016, **27**, 4139–4146.

42 A. A. Zarandi, A. A. S. Alvani, R. Salimi, H. Sameie, S. Moosakhani, D. Poelman and F. Rosei, *J. Mater. Chem. C*, 2015, **3**, 3935–3945.

43 W. Li, Q. Zhang, D. Chen and L. Li, *J. Macromol. Sci., Part A: Pure Appl. Chem.*, 2006, **43**, 1815–1824.

44 Y. Dessie, S. Tadesse, R. Eswaramoorthy and Y. Adimasu, *All Life*, 2021, **14**, 541–568.

45 H. Gul, A.-u.-H. A. Shah, U. Krewer and S. Bilal, *Nanomaterials*, 2020, **10**, 118.

46 A. A. Khan and M. Khalid, *J. Appl. Polym. Sci.*, 2010, **117**, 1601–1607.

47 L. Wang, C. Hu and L. Shao, *Int. J. Nanomed.*, 2017, **12**, 1227.

48 O. S. Ekande and M. Kumar, *J. Environ. Chem. Eng.*, 2021, 105725.

49 S. S. Sambaza, A. Maity and K. Pillay, *ACS Omega*, 2020, **5**, 29642–29656.

50 K. A. Cychosz and M. Thommes, *Engineering*, 2018, **4**, 559–566.

51 S. M. Mousavi-Kouhi, A. Beyk-Khormizi, M. S. Amiri, M. Mashreghi and M. E. T. Yazdi, *Ceram. Int.*, 2021, **47**, 21490–21497.

52 S. Karmakar, Particle Size Distribution and Zeta Potential Based on Dynamic Light Scattering: Techniques to Characterise Stability and Surface distribution of Charged Colloids, *Recent Trends in Materials Physics and Chemistry*, Studium Press (India) Pvt Ltd, 2019, pp. 117–159.

53 B. Konkena and S. Vasudevan, *J. Phys. Chem. Lett.*, 2012, **3**, 867–872.

54 M. Wang, Q. Zhang, W. Hao and Z.-X. Sun, *Chem. Cent. J.*, 2011, **5**, 1–10.

55 R. Mukherjee, R. Sharma, P. Saini and S. De, *Environ. Sci.: Water Res. Technol.*, 2015, **1**, 893–904.

56 L. Ernawati, A. W. Yusariarta, A. D. Laksono, R. A. Wahyuono, H. Widiyandari, R. Rebeka and V. Sitompul, *Nanomaterials*, 2021, **11**(3), 572.

57 N. U. M. Nizam, M. M. Hanafiah, E. Mahmoudi, A. A. Halim and A. W. Mohammad, *Sci. Rep.*, 2021, **11**, 1–17.

58 R. Foroutan, S. J. Peighambardoust, S. H. Peighambardoust, M. Pateiro and J. M. Lorenzo, *Molecules*, 2021, **26**, 2241.

59 S. Chen, J. Zhang, C. Zhang, Q. Yue, Y. Li and C. Li, *Desalination*, 2010, **252**, 149–156.

60 G. F. Abu-Alsoud, K. A. Hawboldt and C. S. Bottaro, *ACS Appl. Mater. Interfaces*, 2020, **12**, 11998–12009.

61 Y. Kuang, X. Zhang and S. Zhou, *Water*, 2020, **12**, 587.

62 O. Ucarli, O. T. Yayintas, M. S. Engin, S. Cay, G. Saglikoglu and S. Yilmaz, *Langmuir*, 2020, **36**, 8265–8271.

63 R. Labied, O. Benturki, A. Y. E. Hamitouche and A. Donnot, *Adsorpt. Sci. Technol.*, 2018, **36**, 1066–1099.

64 A. D. Zand and M. R. Abyaneh, *Sustainable Environ. Res.*, 2020, **30**, 1–16.

65 R. Singh and R. Bhateria, *ACS Omega*, 2020, **5**, 10826–10837.

66 M. A. Al-Ghouti and D. A. Da'ana, *J. Hazard. Mater.*, 2020, **393**, 122383.

67 Q. Hu and Z. Zhang, *J. Mol. Liq.*, 2019, **277**, 646–648.

68 M. Nadiye-Tabbiruka, F. P. Sejie, S. Coetzee and E. Salamula, *J. Adv. Chem.*, 2015, **11**(9), 3959–3972.

69 Y. Miyah, A. Lahrichi, M. Idrissi, S. Boujraf, H. Taouda and F. Zerrouq, *J. Assoc. Arab Univ. Basic Appl. Sci.*, 2017, **23**, 20–28.

70 H. Tian, J. Luo, K. Zhang, C. Ma, Y. Qi, S. Zhan, H. Liu and M. Li, *Nanoscale Res. Lett.*, 2021, **16**(1), 1–12.

71 C.-R. Lin, O. S. Ivanova, D. A. Petrov, A. E. Sokolov, Y.-Z. Chen, M. A. Gerasimova, S. M. Zharkov, Y.-T. Tseng, N. P. Shestakov and I. S. Edelman, *Nanomaterials*, 2021, **11**, 2371.

72 M. Raghu, L. Parashuram, M. Prashanth, K. Y. Kumar, C. P. Kumar and H. Alrobei, *Nano-Struct. Nano-Objects*, 2021, **25**, 100667.

73 M. Rakibuddin, S. Mandal and R. Ananthakrishnan, *New J. Chem.*, 2017, **41**, 1380–1389.

74 D. Prabha, K. Usharani, S. Ilangovan, V. Narasimman, S. Balamurugan, M. Suganya, J. Srivind, V. Nagarethinam and A. Balu, *J. Mater. Sci.: Mater. Electron.*, 2018, **29**, 18708–18717.

75 Y. Wang, A. Zhang, D. Zhang, P. Zhou, R. Wang, J. Xiang, X. Zhang and S. Su, *Colloids Surf., A*, 2019, **579**, 123654.

76 N. Foghahazade, H. Behnejad, M. Mousavi and M. Hamzehloo, *J. Mater. Sci.: Mater. Electron.*, 2020, **31**, 19764–19777.

77 X. Wang, Z. Li, Y. Zhang, Q. Li, H. Du, F. Liu, X. Zhang, H. Mu and J. Duan, *Chem. Eng. J.*, 2022, **429**, 132270.

78 H. R. Kim, A. Razzaq, C. A. Grimes and S.-I. In, *J. CO2 Util.*, 2017, **20**, 91–96.

79 S. Ni, T. Zhou, H. Zhang, Y. Cao and P. Yang, *ACS Appl. Nano Mater.*, 2018, **1**, 5128–5141.

80 W. H. Koppenol, D. M. Stanbury and P. L. Bounds, *Free Radical Biol. Med.*, 2010, **49**, 317–322.

81 H. Alikhani, A. Taherizadeh, M. Kargar and S. J. Mousavi, *J. Mater. Sci.*, 2021, **9**, 90291.

82 K. Pingmuang, J. Chen, W. Kangwansupamonkon, G. G. Wallace, S. Phanichphant and A. Nattestad, *Sci. Rep.*, 2017, **7**, 1–11.

83 Y.-H. Chiu, T.-F. M. Chang, C.-Y. Chen, M. Sone and Y.-J. Hsu, *Catalysts*, 2019, **9**, 430.

84 M. Rochkind, S. Pasternak and Y. Paz, *Molecules*, 2015, **20**, 88–110.

85 M. Srinivas, R. C. Venkata, R. R. Kakarla, N. P. Shetti, M. Reddy and V. R. Anjanapura, *Mater. Res. Express*, 2019, **6**, 125502.

86 W. Yang, D. Wei, X. Jin, C. Xu, Z. Geng, Q. Guo, Z. Ma, D. Dai, H. Fan and X. Yang, *J. Phys. Chem. Lett.*, 2016, **7**, 603–608.

87 Z. Jin, Q. Zhang, J. Chen, S. Huang, L. Hu, Y.-J. Zeng, H. Zhang, S. Ruan and T. Ohno, *Appl. Catal., B*, 2018, **234**, 198–205.

88 E. El-Sharkaway, R. M. Kamel, I. M. El-Sherbiny and S. S. Gharib, *Mater. Adv.*, 2021, **2**, 4497–4531.

89 S. Shahabuddin, N. M. Sarih, F. H. Ismail, M. M. Shahid and N. M. Huang, *RSC Adv.*, 2015, **5**, 83857–83867.

90 Y. Zeng, L. Zhao, W. Wu, G. Lu, F. Xu, Y. Tong, W. Liu and J. Du, *J. Appl. Polym. Sci.*, 2013, **127**, 2475–2482.

91 S. Shahabuddin, N. Muhamad Sarih, S. Mohamad and J. Joon Ching, *Polymers*, 2016, **8**, 27.

92 V. Eskizeybek, F. Sarı, H. Gülce, A. Gülce and A. Avcı, *Appl. Catal., B*, 2012, **119**, 197–206.

93 H. Wu, S. Lin, C. Chen, W. Liang, X. Liu and H. Yang, *Mater. Res. Bull.*, 2016, **83**, 434–441.

94 S. Ameen, H.-K. Seo, M. S. Akhtar and H. S. Shin, *Chem. Eng. J.*, 2012, **210**, 220–228.

95 J. Miao, A. Xie, S. Li, F. Huang, J. Cao and Y. Shen, *Appl. Surf. Sci.*, 2016, **360**, 594–600.

96 E. S. Mansor, H. Ali and A. Abdel-Karim, *Colloid Interface Sci. Commun.*, 2020, **39**, 100314.

97 H. Zhang and Y. Zhu, *J. Phys. Chem. C*, 2010, **114**, 5822–5826.

98 A. K. Sarkar, A. Saha, A. Tarafder, A. B. Panda and S. Pal, *ACS Sustainable Chem. Eng.*, 2016, **4**, 1679–1688.

99 M. Ghaffari-Moghaddam and H. Eslahi, *Arabian J. Chem.*, 2014, **7**, 846–855.

100 K. Kannan, D. Radhika, K. R. Reddy, A. V. Raghu, K. K. Sadasivuni, G. Palani and K. Gurushankar, *Nano Express*, 2021, **2**, 010014.

101 K. Kannan, D. Radhika, A. Nesaraj, K. K. Sadasivuni, K. R. Reddy, D. Kasai and A. V. Raghu, *Mater. Sci. Energy Technol.*, 2020, **3**, 853–861.

102 W. He, H. Jia, J. Cai, X. Han, Z. Zheng, W. G. Wamer and J.-J. Yin, *J. Phys. Chem. C*, 2016, **120**, 3187–3195.

103 J. Robertson, M. Gizdavic-Nikolaidis, M. K. Nieuwoudt and S. Swift, *PeerJ*, 2018, **6**, e5135.

104 A. Mirmohseni, M. Azizi and M. S. S. Dorraji, *Prog. Org. Coat.*, 2020, **139**, 105419.

105 R. Chougale, D. Kasai, S. Nayak, S. Masti, A. Nasalapure and A. V. Raghu, *Green Mater.*, 2019, **8**, 40–48.

106 F. Perreault, A. F. De Faria, S. Nejati and M. Elimelech, *ACS Nano*, 2015, **9**, 7226–7236.

107 X. Liang, M. Sun, L. Li, R. Qiao, K. Chen, Q. Xiao and F. Xu, *Dalton Trans.*, 2012, **41**, 2804–2811.

108 S. S. Rahman, M. M. Rahman, M. Shajahan and A. Al-Mamun, *Design of Efficient Photocatalytic Nanocomposites*

Composed of Manganese Oxides and Graphene Oxide Quantum Dots for Bactericidal Activity: Exploring the Structural and Chemical Roles of Photoactivity, University of California, Santa Cruz, 2021.

109 P. Boomi, H. G. Prabu, P. Manisankar and S. Ravikumar, *Appl. Surf. Sci.*, 2014, **300**, 66–72.

110 A. Shalini, R. Nishanthi, P. Palani and V. Jaisankar, *Mater. Today: Proc.*, 2016, **3**, 1633–1642.

111 G. Kaladevi, P. Wilson and K. Pandian, *Ionics*, 2020, 1–11.

112 H. Yamagata, M. Yoshizawa and M. Minamiyama, *Environ. Monit. Assess.*, 2010, **169**, 67–73.

113 F. Edition, *WHO Chron.*, 2011, **38**, 104–108.